

# Effects of Thermal Boundary Conditions on Natural Convection and Entropy Generation in Non-Newtonian Power-Law Fluids

Lambert Theisen, Satyvir Singh\*

Institute for Applied and Computational Mathematics, RWTH Aachen University, 52062, Aachen, Germany

## ARTICLE INFO

### Keywords:

Natural convection  
Power-law fluids  
Non-Newtonian flow  
Thermal boundary conditions  
Entropy generation  
Finite element method  
Square cavity  
Cylindrical annulus

## ABSTRACT

This study investigates the role of thermal boundary conditions on natural convection and entropy generation in non-Newtonian power-law fluids confined within a square cavity and a concentric cylindrical annulus. Steady, two-dimensional governing equations based on the incompressible power-law model and the Boussinesq approximation are solved using the Gridap.jl finite element framework. The numerical methodology is validated against benchmark solutions for both Newtonian and non-Newtonian convection, showing good agreement in terms of isotherm fields, streamlines, local Nusselt number distributions, and entropy generation. The effects of fluid rheology and heating mode are examined for shear-thinning, Newtonian, and shear-thickening fluids under uniform and non-uniform thermal boundary conditions. The results show that shear-thinning behavior enhances buoyancy-driven circulation, steepens thermal gradients, and increases heat transfer, whereas shear-thickening behavior suppresses convection and promotes conduction-dominated transport. Thermal boundary conditions are found to play an important role in controlling the intensity and spatial distribution of flow, heat transfer, and irreversibility. In both geometries, uniform heating produces stronger and more distributed convective structures, while non-uniform sinusoidal heating localizes thermal forcing and consistently reduces total entropy generation. An entropy analysis further reveals that viscous dissipation dominates irreversibility in shear-thinning fluids, whereas heat-transfer irreversibility becomes dominant as the power-law index increases. The study demonstrates that appropriate thermal boundary design, together with fluid rheology, provides an effective route for controlling heat transfer and minimizing thermodynamic losses in non-Newtonian convection systems. The source code and metadata are publicly available.

## 1. Introduction

Natural convection, driven by buoyancy forces arising from temperature-induced density differences, plays a fundamental role in a wide range of engineering, industrial, and environmental processes, including cooling of electronic equipment, building thermal systems, solar energy applications, and large-scale industrial flows [1–5]. The phenomenon occurs when temperature differences near a heated or cooled surface change the fluid's density. In a gravitational field, the resulting buoyancy forces cause warmer, less dense fluid to rise and cooler, denser fluid to sink, producing flow without external mechanical forcing such as a pump or fan. This passive mode of heat transfer is energy-efficient and has been extensively studied over several decades in both fundamental and applied contexts [6–9]. Despite its apparent simplicity, natural convection involves complex interactions among momentum, energy, and mass conservation mechanisms, particularly when the working fluid exhibits non-Newtonian behavior [10–13].

A wide range of industrial and biological fluids, including polymer solutions, molten plastics, paints, blood, and drilling muds, exhibit non-Newtonian rheological behavior that significantly modifies convective flow dynamics and associated heat transfer characteristics [14–16]. Among the various constitutive models developed to describe such fluids, the power-law (Ostwald–de Waele) model has gained particular prominence due to its simplicity and its ability to represent both shear-thinning ( $n < 1$ ) and shear-thickening ( $n > 1$ ) behaviors through the power-law index  $n$  [11, 17, 18]. In this framework, the apparent viscosity depends on the local shear rate as  $\mu_{\text{eff}} = K\dot{\gamma}^{n-1}$ , where  $K$  denotes the consistency index. The interaction between shear-dependent viscosity and buoyancy-driven momentum transport leads to complex flow structures that differ markedly from those observed in Newtonian fluids, influencing thermal boundary layers and heat transfer rates. Consequently, classical correlations for Newtonian convection are no

\*Corresponding author

✉ [lambert.theisen@rwth-aachen.de](mailto:lambert.theisen@rwth-aachen.de) (L. Theisen); [singh@acom.rwth-aachen.de](mailto:singh@acom.rwth-aachen.de) (S. Singh)  
ORCID(s): 0000-0001-5460-5425 (L. Theisen); 0000-0001-6669-5296 (S. Singh)

longer directly applicable, and dedicated analyses are required [19–21, 54]. Understanding natural convection in power-law fluids is therefore of both fundamental scientific interest and practical importance for the design and optimization of thermal systems involving complex fluids.

Thermal boundary conditions play an important role in determining the flow structure, temperature distribution, and heat transfer characteristics in convective systems. In natural convection problems, the way in which thermal energy is supplied or removed at the boundaries fundamentally governs the buoyancy forces that drive the fluid motion. The most commonly employed thermal boundary conditions in the literature include the isothermal condition, where a uniform constant temperature is maintained at the wall, and the isoflux condition, where a uniform heat flux is prescribed at the boundary [22, 23]. Additionally, more complex conditions such as linearly varying wall temperature, sinusoidal temperature distribution, and mixed or partial heating have been investigated to simulate realistic engineering scenarios [24–26]. Each of these boundary conditions produces different thermal gradients within the fluid domain, resulting in qualitatively and quantitatively different velocity and temperature fields, as well as varying rates of convective heat transfer expressed through the local and average Nusselt number [22, 24, 27].

The choice of thermal boundary condition is not merely a mathematical convenience but reflects the physical reality of the application under consideration. For instance, isothermal boundaries are representative of condensing or evaporating surfaces and highly conductive walls, whereas constant heat flux conditions are more appropriate for electrically heated surfaces, solar collectors, and nuclear reactor cooling channels [23, 28]. In the context of non-Newtonian power-law fluids, the sensitivity to thermal boundary conditions is further amplified because the effective viscosity depends on the local shear rate, which itself is shaped by the temperature-driven velocity gradients near the wall [28, 29]. This two-way coupling between the thermal field and the rheological response makes the selection and analysis of thermal boundary conditions a particularly critical aspect of non-Newtonian convection studies [30, 31]. Consequently, a systematic comparison of different thermal boundary conditions is essential to develop a comprehensive understanding of heat transfer behavior in power-law fluid systems and to provide reliable guidelines for practical thermal engineering design [32, 33].

The second law of thermodynamics provides an additional framework for evaluating the performance of thermal systems beyond what is possible through energy conservation alone. Entropy generation, which quantifies the irreversibility associated with heat transfer, viscous dissipation, and mass transfer within a system, serves as a direct measure of the thermodynamic inefficiency of a convective process [34]. The concept was first introduced by Adrian Bejan [35], who showed that minimizing entropy generation provides a fundamental basis for the design of thermally optimal systems. In buoyancy-driven convective flows, entropy is generated due to two primary mechanisms: irreversibility arising from finite temperature gradients, referred to as thermal entropy generation, and irreversibility due to fluid friction, referred to as viscous entropy generation [34, 36]. The relative dominance of these two contributions is conveniently characterized by the Bejan number, defined as the ratio of thermal entropy generation to total entropy generation, which approaches unity when heat transfer irreversibility dominates and tends toward zero when viscous dissipation effects prevail [35, 36]. A thorough understanding of entropy generation and its spatial distribution within the flow domain is therefore essential for identifying thermodynamically inefficient regions and guiding the design of energy-optimal thermal systems.

In the context of non-Newtonian power-law fluids, entropy generation analysis acquires additional complexity due to the nonlinear dependence of the effective viscosity on the local shear rate. Unlike Newtonian fluids where viscous dissipation is governed by a constant dynamic viscosity, the spatially varying effective viscosity in power-law fluids introduces a strong coupling between the flow kinematics and the local entropy production rate [38, 39]. For shear-thinning fluids, the reduced effective viscosity in high-shear regions tends to suppress viscous entropy generation while simultaneously enhancing convective heat transfer, whereas shear-thickening fluids exhibit the opposite trend, with elevated viscosity amplifying frictional irreversibilities [38]. Furthermore, the thermal boundary conditions imposed on the enclosure walls directly govern the temperature gradients within the fluid domain, thereby modulating the magnitude and spatial distribution of thermal entropy generation [32, 36]. Consequently, a systematic entropy generation analysis that accounts for the combined effects of power-law rheology and thermal boundary conditions is indispensable for a complete thermodynamic characterization of non-Newtonian natural convection systems, and this interplay remains an open and active area of research [32, 39].

The study of natural convection in non-Newtonian fluids has experienced remarkable growth over the past few decades, driven by the increasing demand for accurate thermal modeling in polymer processing, food engineering, and biomedical applications. Early investigations by Acrivos et al. [40] established the theoretical foundations of boundary layer natural convection for power-law fluids past heated surfaces, demonstrating that the power-law index significantly

alters the velocity and temperature boundary layer thicknesses. Subsequent numerical and analytical studies extended these findings to enclosed cavities, with significant contributions from Ozoe and Churchill [41], who examined the influence of rheological behavior on heat transfer rates in differentially heated enclosures. A major advancement was made by Turan et al. [42], who performed systematic two-dimensional steady-state simulations of laminar natural convection of power-law fluids in square enclosures with differentially heated sidewalls subjected to constant wall temperatures, providing detailed correlations between the mean Nusselt number, Rayleigh number, Prandtl number, and power-law index. The same group further extended their analysis to constant wall heat flux boundary conditions [43], demonstrating that the choice of thermal boundary condition leads to quantitatively distinct heat transfer scaling behaviors, particularly for strongly shear-thinning fluids. These foundational contributions collectively confirmed that non-Newtonian rheology introduces qualitatively distinct flow patterns and heat transfer mechanisms compared to classical Newtonian natural convection, necessitating dedicated computational frameworks tailored to power-law constitutive behavior [44, 45].

More recent investigations have increasingly focused on the combined role of thermal boundary conditions, enclosure geometry, and rheological nonlinearity in governing the convective behavior of power-law fluids. Lamsaadi et al. [45] examined natural convection of power-law fluids in a shallow horizontal rectangular cavity subjected to uniform heat flux boundary conditions, demonstrating that shear-thinning fluids exhibit enhanced heat transfer under isoflux conditions compared to isothermal heating. The influence of sinusoidal and non-uniform thermal boundary conditions on power-law fluid convection in square and trapezoidal cavities has been explored by Basak and co-workers [25, 28], with results indicating that the spatial periodicity of the wall temperature distribution leads to multiple convective cell formations and non-monotonic Nusselt number variations. More recently, numerical studies on power-law nanofluids in square cavities with internal fins under different thermal boundary conditions [29] confirmed that the Nusselt number enhancement is strongly amplified for shear-thinning nanofluids, with improvements exceeding 130% compared to Newtonian behavior at high Rayleigh numbers. Further contributions using multigrid solvers [31] have reinforced the sensitivity of flow structures and thermal irreversibilities to the imposed boundary conditions in power-law fluid systems. Despite these advances, a systematic and comprehensive comparative study that simultaneously examines the effects of multiple thermal boundary conditions on both the convective heat transfer and the entropy generation characteristics of power-law fluids remains scarce in the open literature [32, 36], thereby motivating the present work.

Despite the considerable body of literature on natural convection in power-law fluids, a critical examination reveals several important gaps that remain unaddressed. The majority of earlier investigations have treated flow behavior, heat transfer, and entropy generation as largely separate problems, with very few studies considering these quantities within a unified analysis framework [32, 36]. While the influence of thermal boundary conditions on Newtonian natural convection has been extensively documented [22–24], the corresponding systematic analysis for non-Newtonian power-law fluids subjected to multiple distinct thermal boundary conditions remains largely absent [42, 43]. Moreover, entropy generation studies for power-law fluids that simultaneously account for rheological nonlinearity, power-law index effects, and the type of imposed thermal boundary condition are scarce in the open literature [32, 38, 39].

To address these gaps, the specific objectives of the present work are: (i) to develop and validate a robust finite element solver for steady-state laminar natural convection of power-law fluids in a square cavity and a concentric cylindrical annulus [22, 42]; (ii) to investigate the combined influence of the power-law index  $n$  and thermal boundary conditions, including uniform and non-uniform heating, on the flow structure and heat transfer characteristics expressed through local and average Nusselt numbers [23, 42, 43]; (iii) to evaluate the spatial distribution of local entropy generation due to heat transfer and viscous dissipation, total entropy generation, and average Bejan number across a range of power-law indices and thermal boundary conditions [32, 34, 35]; and (iv) to provide physical insight into the interplay between shear-thinning ( $n < 1$ ), Newtonian ( $n = 1$ ), and shear-thickening ( $n > 1$ ) behaviors and the imposed thermal boundary conditions on heat-transfer performance and thermodynamic irreversibility [36, 38]. The findings of this study are expected to contribute to the optimization of energy-efficient thermal systems involving complex fluids and diverse enclosure designs.

The remainder of this manuscript is organized as follows. Section 2 presents the mathematical formulation, including the governing equations, thermal boundary conditions, and power-law constitutive model. Section 3 describes the finite element framework and nonlinear solution strategy. Then, Section 4 introduces the post-processing quantities, including the stream function, heat function, Nusselt number, entropy generation, and Bejan number. Validation studies for both Newtonian and non-Newtonian natural convection, benchmarked against established results from the literature, are presented in Section 5. The effects of the power-law index and thermal boundary conditions on flow structure, heat

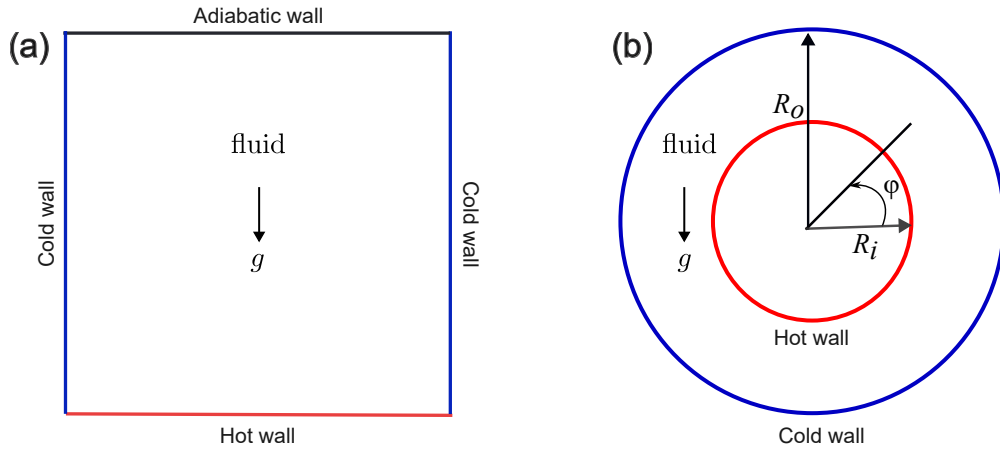


**Figure 1:** Schematic diagrams of the physical domains considered in the study of natural convection and entropy generation in power-law fluids. (a) Square cavity with a hot bottom wall, cold vertical side walls, and an adiabatic top wall. (b) Concentric cylindrical annulus with an inner hot cylinder of radius  $R_i$  and an outer cold cylinder of radius  $R_o$ , where  $\varphi$  denotes the angular coordinate. In both configurations, the gravitational acceleration  $g$  acts vertically downward.

transfer, and entropy generation in both geometries are discussed in Section 6. Finally, the key conclusions and outlook of this study are summarized in Section 7.

## 2. Mathematical formulation

### 2.1. Problem Setup

This study investigates steady-state natural convection and entropy generation in non-Newtonian power-law fluids confined within two distinct two-dimensional geometrical configurations, including a square cavity and a concentric cylindrical annulus, as illustrated in Figure 1. In both configurations, the flow is driven by buoyancy forces arising from temperature differences imposed at the domain boundaries, and the gravitational acceleration  $g$  acts vertically downward. In the square cavity configuration, shown in Fig. 1(a), the computational domain is a unit square filled with a power-law fluid. The bottom wall is subjected to either uniform heating or non-uniform sinusoidal heating, representing the hot wall, while the top wall is thermally insulated, i.e., adiabatic with zero heat flux. The two vertical side walls are maintained at a constant lower temperature, serving as the cold walls. The imposed temperature difference between the hot bottom wall and the cold side walls drives the buoyancy-induced fluid motion within the enclosure. In the concentric cylindrical annulus configuration, shown in Fig. 1(b), the fluid occupies the annular region between two coaxial cylinders. The inner cylinder of radius  $R_i$  is subjected to either uniform heating or non-uniform sinusoidal heating, while the outer cylinder of radius  $R_o$  is kept at a lower constant temperature (cold wall), with the characteristic length defined as the gap width  $L = R_o - R_i$ . The angular coordinate  $\varphi$  describes the circumferential direction of flow within the annular domain. Natural convection patterns are driven by the radial temperature gradient between the inner hot and outer cold cylinders, with gravity acting vertically downward.

### 2.2. Governing equations

The present study investigates steady-state, two-dimensional, laminar natural convection of an incompressible non-Newtonian power-law fluid confined within a square cavity and a concentric cylindrical annulus. The flow is driven by buoyancy forces induced by temperature gradients imposed through thermal boundary conditions. The governing equations for the flow and thermal fields are formulated based on the conservation of mass, momentum, and energy under the assumptions that the fluid is incompressible with constant thermophysical properties and that the Boussinesq approximation is valid, whereby density variations are considered only in the buoyancy term while neglected elsewhere. Furthermore, thermal radiation is neglected, and viscous heating is omitted from the energy equation; the associated fluid-friction irreversibility is evaluated separately in the entropy-generation post-processing. Under these assumptions,

the dimensional governing equations in Cartesian coordinates  $(x, y)$  are given as follows [22],

$$\frac{\partial u}{\partial x} + \frac{\partial v}{\partial y} = 0, \quad (1)$$

$$\rho \left( u \frac{\partial u}{\partial x} + v \frac{\partial u}{\partial y} \right) = -\frac{\partial p}{\partial x} + \frac{\partial \tau_{xx}}{\partial x} + \frac{\partial \tau_{xy}}{\partial y}, \quad (2)$$

$$\rho \left( u \frac{\partial v}{\partial x} + v \frac{\partial v}{\partial y} \right) = -\frac{\partial p}{\partial y} + \frac{\partial \tau_{xy}}{\partial x} + \frac{\partial \tau_{yy}}{\partial y} + \rho g \beta (T - T_c), \quad (3)$$

$$\rho c_p \left( u \frac{\partial T}{\partial x} + v \frac{\partial T}{\partial y} \right) = \kappa \left( \frac{\partial^2 T}{\partial x^2} + \frac{\partial^2 T}{\partial y^2} \right), \quad (4)$$

where  $(u, v)$  are the velocity components,  $p$  is the pressure,  $T$  is the temperature,  $\rho$  is the fluid density,  $g$  is the gravitational acceleration,  $\beta$  is the thermal expansion coefficient,  $\kappa$  is the thermal conductivity,  $c_p$  is the specific heat capacity, and  $\tau_{ij}$  is the shear stress tensor.

### 2.3. Power-Law Constitutive Model

The rheological behavior of the working fluid is described by the power-law (Ostwald–de Waele) constitutive equation [37]. The shear stress tensor  $\boldsymbol{\tau} \in \mathbb{R}^{2 \times 2}$  is defined as

$$\tau_{ij} = 2\mu_a D_{ij}, \quad D_{ij} = \frac{1}{2} \left( \frac{\partial u_i}{\partial x_j} + \frac{\partial u_j}{\partial x_i} \right), \quad (5)$$

where  $D_{ij}$  are the components of the rate-of-deformation tensor  $\mathbf{D}$ , and  $\mu_a$  is the apparent dynamic viscosity defined as

$$\mu_a = K (2\mathbf{D} : \mathbf{D})^{\frac{n-1}{2}} = K \left\{ 2 \left[ \left( \frac{\partial u}{\partial x} \right)^2 + \left( \frac{\partial v}{\partial y} \right)^2 \right] + \left( \frac{\partial u}{\partial y} + \frac{\partial v}{\partial x} \right)^2 \right\}^{\frac{n-1}{2}}, \quad (6)$$

where  $K > 0$  is the consistency coefficient and  $n > 0$  is the power-law index. The model recovers a Newtonian fluid with constant viscosity  $\mu = K$  for  $n = 1$ .

### 2.4. Non-Dimensionalization

The governing equations are cast in dimensionless form using the following reference scales. The cavity side length (or gap width for the annulus)  $L$  is chosen as the length scale, the thermal diffusivity-based velocity  $\alpha/L$  as the velocity scale,  $T_h$  and  $T_c$  are the temperatures at hot and cold walls, respectively, and  $\rho(\alpha/L)^2$  as the pressure scale [54, 55].

$$X = \frac{x}{L}, \quad Y = \frac{y}{L}, \quad U = \frac{uL}{\alpha}, \quad V = \frac{vL}{\alpha}, \quad \theta = \frac{T - T_c}{T_h - T_c}, \quad P = \frac{pL^2}{\rho\alpha^2}. \quad (7)$$

The apparent viscosity is scaled by the shear rate associated with the diffusive velocity scale, such that  $\mu_a = K(\alpha/L^2)^{n-1} \bar{\mu}$ . The resulting dimensionless apparent viscosity is

$$\bar{\mu} = \left\{ 2 \left[ \left( \frac{\partial U}{\partial X} \right)^2 + \left( \frac{\partial V}{\partial Y} \right)^2 \right] + \left( \frac{\partial U}{\partial Y} + \frac{\partial V}{\partial X} \right)^2 \right\}^{\frac{n-1}{2}}, \quad (8)$$

and the modified Prandtl and Rayleigh numbers for power-law fluids are defined following Ng and Hartnett's convention as used by Turan et al. [54] and Matin and Khan [55]:

$$\text{Pr} = \frac{K}{\rho} \frac{L^{2-2n}}{\alpha^{2-n}}, \quad \text{Ra} = \frac{g\beta\Delta T L^{2n+1}}{(K/\rho)\alpha^n}, \quad (9)$$

where  $\alpha = \kappa/(\rho c_p)$  is the thermal diffusivity and  $\Delta T = T_h - T_c$ . For  $n = 1$ , these definitions reduce to the classical Newtonian forms  $\text{Pr} = \nu/\alpha$  and  $\text{Ra} = g\beta\Delta T L^3/(\nu\alpha)$  with  $\nu = K/\rho$ . Substituting Eqs. (7)–(9) into Eqs. (1)–(4), the dimensionless governing equations become

$$\frac{\partial U}{\partial X} + \frac{\partial V}{\partial Y} = 0, \quad (10)$$

$$U \frac{\partial U}{\partial X} + V \frac{\partial U}{\partial Y} = -\frac{\partial P}{\partial X} + \text{Pr} \left[ 2 \frac{\partial}{\partial X} \left( \bar{\mu} \frac{\partial U}{\partial X} \right) + \frac{\partial}{\partial Y} \left( \bar{\mu} \left( \frac{\partial U}{\partial Y} + \frac{\partial V}{\partial X} \right) \right) \right], \quad (11)$$

$$U \frac{\partial V}{\partial X} + V \frac{\partial V}{\partial Y} = -\frac{\partial P}{\partial Y} + \text{Pr} \left[ \frac{\partial}{\partial X} \left( \bar{\mu} \left( \frac{\partial U}{\partial Y} + \frac{\partial V}{\partial X} \right) \right) + 2 \frac{\partial}{\partial Y} \left( \bar{\mu} \frac{\partial V}{\partial Y} \right) \right] + \text{Ra Pr } \theta, \quad (12)$$

$$U \frac{\partial \theta}{\partial X} + V \frac{\partial \theta}{\partial Y} = \frac{\partial^2 \theta}{\partial X^2} + \frac{\partial^2 \theta}{\partial Y^2}. \quad (13)$$

In vector notation, the buoyancy term appearing in the vertical momentum equation is written as  $\text{Ra Pr } \theta \hat{\mathbf{g}}$ , where  $\hat{\mathbf{g}} = (0, 1)^\top$  denotes the dimensionless buoyancy direction, opposite to the downward gravitational acceleration.

## 2.5. Boundary Conditions

The dimensionless boundary conditions corresponding to Eqs. (10)–(13) are prescribed according to the geometry under consideration. For the square cavity, the boundary conditions are given by

$$\begin{cases} U = V = 0 & \text{on all walls (no-slip),} \\ \theta(X, 0) = 1 & \text{(uniform heating) or } \theta(X, 0) = \sin(\pi X) & \text{(non-uniform heating),} \\ \theta(0, Y) = \theta(1, Y) = 0 & \text{(cold side walls),} \\ \frac{\partial \theta}{\partial Y}(X, 1) = 0 & \text{(adiabatic top wall).} \end{cases} \quad (14)$$

For the concentric cylindrical annulus, the corresponding boundary conditions are expressed as

$$\begin{cases} U = V = 0, & \text{on all walls (no-slip),} \\ \theta = 0 & \text{at } r = R_o \text{ (cold outer wall),} \\ U = V = 0, \quad \theta = 1 & \text{(uniform heating) or} \\ \theta = 0.5(1 + \sin \varphi) & \text{(non-uniform heating) at } r = R_i \text{ (hot inner wall).} \end{cases} \quad (15)$$

## 3. Finite element framework and numerical solution

To obtain a numerical solution of the dimensionless governing Eqs. (10)–(13) subject to the boundary conditions (14)–(15), the Galerkin finite element method (FEM) is employed. The implementation is carried out using the `Gridap.jl` finite element framework [46, 47] within the Julia programming language [48]. The computational domain  $\Omega$  is partitioned into a finite number of non-overlapping elements, and the continuous solution fields are approximated using polynomial basis functions within each element. The full derivation of the weak formulation is provided in Appendix B. For reproducibility, the source code and all metadata are available at [57].

### 3.1. Element Choice and Discrete Approximation

Taylor–Hood finite elements are employed, which consist of continuous second-order Lagrange polynomials for the velocity components ( $U, V$ ) and temperature  $\theta$ , and continuous first-order Lagrange polynomials for the pressure  $P$ . The pressure space is constrained to have zero mean over the computational domain, which fixes the pressure null space associated with the incompressible formulation. This inf-sup stable element pair ensures a well-posed discrete velocity-pressure coupling and avoids spurious pressure modes. The discrete solution fields are expressed as linear combinations of nodal basis functions

$$U_h(\mathbf{x}) = \sum_{i=1}^{N_u} U_i \Phi_i^u(\mathbf{x}), \quad V_h(\mathbf{x}) = \sum_{i=1}^{N_u} V_i \Phi_i^v(\mathbf{x}), \quad P_h(\mathbf{x}) = \sum_{i=1}^{N_p} P_i \Phi_i^p(\mathbf{x}), \quad \theta_h(\mathbf{x}) = \sum_{i=1}^{N_\theta} \theta_i \Phi_i^\theta(\mathbf{x}), \quad (16)$$

where  $U_i, V_i, P_i,$  and  $\theta_i$  are the nodal degrees of freedom (DOFs);  $\Phi_i^u, \Phi_i^v,$  and  $\Phi_i^\theta$  are the basis functions for velocity, pressure, and temperature, respectively; and  $N_u, N_p,$  and  $N_\theta$  denote the total number of velocity, pressure, and temperature DOFs. Dirichlet boundary conditions are imposed through affine trial spaces for velocity and temperature, whereas the corresponding test spaces satisfy homogeneous Dirichlet conditions. In the Galerkin method, the test functions use the same polynomial orders as the trial functions, and testing with the basis functions leads to a system of algebraic equations for the nodal DOFs as detailed in the next section.

### 3.2. Discrete Residual Equations

Substituting the discrete approximations (16) into the weak formulation (see Appendix B) yields the discrete nonlinear residual vector  $\mathbf{R} = (\mathbf{R}_U, \mathbf{R}_V, \mathbf{R}_P, \mathbf{R}_\theta)^\top$ , whose components are computed as follows

$$\begin{aligned} R_{U,i} = & \sum_{j=1}^{N_u} U_j \int_{\Omega} \left( U_h \frac{\partial \Phi_j^u}{\partial X} + V_h \frac{\partial \Phi_j^u}{\partial Y} \right) \Phi_i^u \, d\Omega - \sum_{j=1}^{N_p} P_j \int_{\Omega} \Phi_j^p \frac{\partial \Phi_i^u}{\partial X} \, d\Omega \\ & + 2Pr \sum_{j=1}^{N_u} U_j \int_{\Omega} \bar{\mu}_s \frac{\partial \Phi_j^u}{\partial X} \frac{\partial \Phi_i^u}{\partial X} \, d\Omega + Pr \sum_{j=1}^{N_u} \int_{\Omega} \bar{\mu}_s \left( U_j \frac{\partial \Phi_j^u}{\partial Y} + V_j \frac{\partial \Phi_j^u}{\partial X} \right) \frac{\partial \Phi_i^u}{\partial Y} \, d\Omega, \end{aligned} \quad (17)$$

$$\begin{aligned} R_{V,i} = & \sum_{j=1}^{N_u} V_j \int_{\Omega} \left( U_h \frac{\partial \Phi_j^u}{\partial X} + V_h \frac{\partial \Phi_j^u}{\partial Y} \right) \Phi_i^u \, d\Omega - \sum_{j=1}^{N_p} P_j \int_{\Omega} \Phi_j^p \frac{\partial \Phi_i^u}{\partial Y} \, d\Omega \\ & + Pr \sum_{j=1}^{N_u} \int_{\Omega} \bar{\mu}_s \left( U_j \frac{\partial \Phi_j^u}{\partial Y} + V_j \frac{\partial \Phi_j^u}{\partial X} \right) \frac{\partial \Phi_i^u}{\partial X} \, d\Omega + 2Pr \sum_{j=1}^{N_u} V_j \int_{\Omega} \bar{\mu}_s \frac{\partial \Phi_j^u}{\partial Y} \frac{\partial \Phi_i^u}{\partial Y} \, d\Omega \\ & - Ra Pr \sum_{j=1}^{N_\theta} \theta_j \int_{\Omega} \Phi_j^\theta \Phi_i^u \, d\Omega, \end{aligned} \quad (18)$$

$$R_{P,i} = \sum_{j=1}^{N_u} U_j \int_{\Omega} \frac{\partial \Phi_j^u}{\partial X} \Phi_i^p \, d\Omega + \sum_{j=1}^{N_u} V_j \int_{\Omega} \frac{\partial \Phi_j^u}{\partial Y} \Phi_i^p \, d\Omega, \quad (19)$$

$$R_{\theta,i} = \sum_{j=1}^{N_\theta} \theta_j \int_{\Omega} \left( U_h \frac{\partial \Phi_j^\theta}{\partial X} + V_h \frac{\partial \Phi_j^\theta}{\partial Y} \right) \Phi_i^\theta \, d\Omega + \sum_{j=1}^{N_\theta} \theta_j \int_{\Omega} \left( \frac{\partial \Phi_j^\theta}{\partial X} \frac{\partial \Phi_i^\theta}{\partial X} + \frac{\partial \Phi_j^\theta}{\partial Y} \frac{\partial \Phi_i^\theta}{\partial Y} \right) \, d\Omega. \quad (20)$$

Note that in Eqs. (17)–(20),  $U_h$  and  $V_h$  are the discrete velocity fields from (16) evaluated at the current iterate, which enter the convective terms nonlinearly. The viscosity term  $\bar{\mu}_s$  also depends nonlinearly on the discrete velocity field through the stabilized form of Eq. (8), as detailed in Appendix B, making the overall system highly nonlinear, particularly for strongly shear-thinning ( $n \ll 1$ ) or shear-thickening ( $n \gg 1$ ) fluids. The resulting system of nonlinear algebraic equations is solved using either the Newton–Raphson method or the trust-region method implemented in the `NLsolve.jl` package [49], as described in the following sections.

### 3.3. Newton–Raphson Solution Method

The discrete nonlinear system  $\mathbf{R}(\mathbf{U}_h) = \mathbf{0}$  is solved using the Newton–Raphson method. The global DOF vector is

$$\mathbf{U}_h = \left( U_1, \dots, U_{N_u}, V_1, \dots, V_{N_u}, P_1, \dots, P_{N_p}, \theta_1, \dots, \theta_{N_\theta} \right)^\top \in \mathbb{R}^{N_{\text{dof}}}, \quad (21)$$

where  $N_{\text{dof}} = 2N_u + N_p + N_\theta$  is the total number of degrees of freedom. After the prescribed Dirichlet data have been incorporated into the affine trial spaces, the free unknowns are initialized by a zero vector. At each Newton iteration  $k = 0, 1, 2, \dots$ , the linearized system

$$\mathbf{J}^{(k)} \delta \mathbf{U}_h^{(k)} = -\mathbf{R}^{(k)}, \quad (22)$$

is solved for the update  $\delta \mathbf{U}_h^{(k)}$ , where  $\mathbf{J}^{(k)} = (\partial \mathbf{R} / \partial \mathbf{U}_h) |_{\mathbf{U}_h^{(k)}}$  is the discrete Jacobian matrix evaluated at the current iterate  $\mathbf{U}_h^{(k)}$  and  $\mathbf{R}^{(k)}$  is the residual at the same iterate. The Jacobian has the block structure

$$\mathbf{J}^{(k)} = \begin{bmatrix} \mathbf{J}_{UU}^{(k)} & \mathbf{J}_{UV}^{(k)} & \mathbf{J}_{UP}^{(k)} & \mathbf{0} \\ \mathbf{J}_{VU}^{(k)} & \mathbf{J}_{VV}^{(k)} & \mathbf{J}_{VP}^{(k)} & \mathbf{J}_{V\theta}^{(k)} \\ \mathbf{J}_{PU}^{(k)} & \mathbf{J}_{PV}^{(k)} & \mathbf{0} & \mathbf{0} \\ \mathbf{J}_{\theta U}^{(k)} & \mathbf{J}_{\theta V}^{(k)} & \mathbf{0} & \mathbf{J}_{\theta\theta}^{(k)} \end{bmatrix}, \quad (23)$$

where each block represents the coupling between field variables  $A$  and  $B$ , computed analytically from the derivatives of the residual components in Eqs. (17)–(20). The zero blocks  $\mathbf{J}_{U\theta}^{(k)} = \mathbf{0}$ ,  $\mathbf{J}_{PP}^{(k)} = \mathbf{0}$ ,  $\mathbf{J}_{P\theta}^{(k)} = \mathbf{0}$ , and  $\mathbf{J}_{\theta P}^{(k)} = \mathbf{0}$  reflect, respectively, the absence of temperature coupling in the horizontal momentum equation, the absence of pressure in the continuity Eq. (19), the absence of temperature in the continuity Eq. (19), and the decoupling of pressure from the energy Eq. (20). The solution is then updated as

$$\mathbf{U}_h^{(k+1)} = \mathbf{U}_h^{(k)} + \delta \mathbf{U}_h^{(k)}, \quad (24)$$

and iterations continue until the convergence criterion

$$\|\mathbf{R}^{(k)}\|_{\infty} \leq \varepsilon_{\mathbf{R}} = 10^{-10} \quad (25)$$

The linear systems (22) are solved at each iteration using a direct LU decomposition.

### 3.4. Trust-Region Method

As an alternative to the standard Newton–Raphson approach, the discrete trust-region method is also employed. In our computational studies, the trust-region method achieved better convergence for specific cases involving poor initial guesses or ill-conditioned discrete Jacobian matrices, particularly at extreme power-law indices ( $n \ll 1$  or  $n \gg 1$ ) and high Rayleigh numbers. At each iteration  $k$ , the algorithm constructs a local linear model of the discrete residual

$$m_k(\mathbf{p}) = \mathbf{R}^{(k)} + \mathbf{J}^{(k)}\mathbf{p}, \quad (26)$$

and approximately minimizes the corresponding trust-region least-squares subproblem

$$\min_{\mathbf{p} \in \mathbb{R}^{N_{\text{dof}}}} \|\mathbf{R}^{(k)} + \mathbf{J}^{(k)}\mathbf{p}\|_2^2 \quad \text{subject to} \quad \|\mathbf{D}_k \mathbf{p}\|_2 \leq \Delta_k, \quad (27)$$

which corresponds to a local quadratic least-squares model for the residual norm. Here,  $\Delta_k > 0$  is the trust-region radius and  $\mathbf{D}_k$  is a diagonal scaling matrix. In the computations reported here, the subproblem is treated by the dogleg strategy used in `NLSolve.jl`: the algorithm first tests the full Gauss–Newton step, and if it lies outside the trust region, it uses either the Cauchy step or an interpolated step along the dogleg path. The step is accepted or rejected based on the ratio of actual to predicted reduction in the residual norm

$$\rho_k = \frac{\|\mathbf{R}^{(k)}\|_2^2 - \|\mathbf{R}^{(k+1)}\|_2^2}{\|\mathbf{R}^{(k)}\|_2^2 - \|m_k(\mathbf{p}_k)\|_2^2}. \quad (28)$$

If  $\rho_k$  is sufficiently positive, the step is accepted and the Jacobian is updated at the new iterate; otherwise, the step is rejected and the previous iterate is restored. The trust-region radius is reduced when the model prediction is poor and enlarged when the prediction is accurate and the accepted step is close to the trust-region boundary. This adaptive mechanism improves robustness for the strongly nonlinear problems arising from the power-law viscosity term  $\bar{\mu}_s(\mathbf{U}_h)$  in the discrete finite element formulation, where the standard Newton–Raphson method may fail to converge.

## 4. Post-processing of heat transfer and flow quantities

After obtaining the discrete solution  $(\mathbf{U}_h, P_h, \theta_h)$ , key physical quantities are evaluated in a post-processing step. These include the stream function  $\psi_h$ , the heat function  $\Pi_h$ , the Nusselt numbers, the entropy generation rates, and the Bejan number, which together characterize the flow structure, the heat transfer, and the thermodynamic irreversibility.

### 4.1. Stream Function

The stream function  $\psi_h$  is used to visualize the fluid motion through streamlines. For a two-dimensional incompressible flow, the velocity components  $(U_h, V_h)$  are related to the stream function,

$$U_h = \frac{\partial \psi_h}{\partial Y}, \quad V_h = -\frac{\partial \psi_h}{\partial X}, \quad (29)$$

which, after taking another derivative to the terms in (29), yields the Poisson problem for  $\psi_h$ , namely,

$$\frac{\partial^2 \psi_h}{\partial X^2} + \frac{\partial^2 \psi_h}{\partial Y^2} = \frac{\partial U_h}{\partial Y} - \frac{\partial V_h}{\partial X}. \quad (30)$$

Therefore, the discrete stream function  $\psi_h$  is obtained by solving the following weak formulation: Find  $\psi_h \in H_0^1(\Omega)$  (where  $H_0^1(\Omega)$  denotes a function space with zero boundary conditions) such that for all  $\xi \in H_0^1(\Omega)$

$$\int_{\Omega} \nabla \psi_h \cdot \nabla \xi \, d\Omega = \int_{\Omega} \left( \frac{\partial V_h}{\partial X} - \frac{\partial U_h}{\partial Y} \right) \xi \, d\Omega = \int_{\Omega} (\mathbf{R} \nabla U_h) \xi \, d\Omega, \quad (31)$$

with the rotation matrix

$$\mathbf{R} = \begin{pmatrix} 0 & -1 \\ 1 & 0 \end{pmatrix}. \quad (32)$$

The homogeneous Dirichlet condition  $\psi_h = 0$  on  $\partial\Omega$  follows directly from the no-slip condition  $\mathbf{u} = \mathbf{0}$  on  $\partial\Omega$ . The discrete problem is solved using first-order Lagrange finite elements. By convention (29), a positive value of  $\psi_h$  indicates counter-clockwise circulation, while a negative value indicates clockwise circulation.

## 4.2. Heat Function

The heat function  $\Pi_h$ , similar to  $\psi_h$ , provides a visualization of the total heat flow within the enclosure by combining conductive and advective heat fluxes. The total heat flux vector is defined as follows,

$$\mathbf{q}_{\text{tot}} = \mathbf{q}_{\text{adv}} + \mathbf{q}_{\text{cond}} = \mathbf{U}_h \theta_h - \nabla \theta_h, \quad (33)$$

and the isolines of  $\Pi_h$  coincide with the trajectories of  $\mathbf{q}_{\text{tot}}$ . Equivalently, the gradient of the heat function is orthogonal to the total heat flux.

$$\nabla \Pi_h \cdot \mathbf{q}_{\text{tot}} = 0, \quad \nabla \Pi_h = \sigma \mathbf{R} \mathbf{q}_{\text{tot}}, \quad (34)$$

with  $\mathbf{R}$  from Eq. (32) and  $\sigma \in \{-1, +1\}$ . To fix the sign convention such that  $\Pi_h > 0$  for anti-clockwise heat flow [50–52], we set  $\sigma = -1$ . Taking the negative divergence of Eq. (34) yields the following Poisson problem

$$-\nabla^2 \Pi_h = \nabla \cdot (\mathbf{R} \mathbf{q}_{\text{tot}}) = \nabla \cdot [\mathbf{R}(\mathbf{U}_h \theta_h - \nabla \theta_h)], \quad (35)$$

whose weak formulation reads: given  $\theta_h$  and  $\mathbf{U}_h$ , find  $\Pi_h \in H_{\Gamma_D}^1(\Omega)$  such that for all  $\xi \in H_0^1(\Omega)$

$$\int_{\Omega} \nabla \Pi_h \cdot \nabla \xi \, d\Omega = - \int_{\Omega} \mathbf{R} (\mathbf{U}_h \theta_h - \nabla \theta_h) \cdot \nabla \xi \, d\Omega. \quad (36)$$

The heat function is determined only up to an additive constant unless a reference value is prescribed. In the implementation, zero Dirichlet values are imposed on the selected heat-function reference tags: these are the adiabatic-wall tags for the square-cavity cases and designated reference-point tags for the annular cases. Homogeneous natural conditions are used on the remaining boundary. This fixes the constant and gives a unique discrete heat function. By convention, a positive  $\Pi_h$  denotes anti-clockwise heat flow and a negative  $\Pi_h$  denotes clockwise heat flow.

## 4.3. Nusselt Number

The Nusselt number quantifies the dimensionless heat flux at the domain boundary. On a boundary  $\partial\Omega$  with unit normal  $\mathbf{n}$ , the local Nusselt number is defined from the normal temperature gradient as

$$\text{Nu}(\mathbf{x}) = \left| \frac{\partial \theta_h}{\partial \mathbf{n}} \right| = |\nabla \theta_h(\mathbf{x}) \cdot \mathbf{n}|. \quad (37)$$

For the square cavity, the local Nusselt numbers on the bottom and side walls are therefore

$$\text{Nu}_b(X) = \left| \frac{\partial \theta_h}{\partial Y}(X, 0) \right|, \quad \text{Nu}_s(Y) = \left| \frac{\partial \theta_h}{\partial X}(X_s, Y) \right|, \quad X_s \in \{0, 1\}. \quad (38)$$

The corresponding average Nusselt numbers are obtained by integration along the respective walls,

$$\overline{\text{Nu}}_b = \int_0^1 \text{Nu}_b(X) dX, \quad \overline{\text{Nu}}_s = \int_0^1 \text{Nu}_s(Y) dY. \quad (39)$$

For the concentric cylindrical annulus, the local and average Nusselt numbers on a cylindrical wall is computed from the radial temperature gradient,

$$\text{Nu}_r(r, \varphi) = \left| \frac{\partial \theta_h}{\partial r}(r, \varphi) \right|, \quad \overline{\text{Nu}}^{\text{in}} = \frac{1}{2\pi} \int_0^{2\pi} \text{Nu}_r(R_i, \varphi) d\varphi. \quad (40)$$

#### 4.4. Entropy Generation

Thermodynamic irreversibilities in natural convection systems arise from two sources: heat transfer across finite temperature gradients and viscous dissipation due to fluid friction [34]. Following the dimensionless entropy generation measures used by Kaluri and Basak [53], the local heat-transfer and fluid-friction contributions in Cartesian coordinates  $(X, Y)$  are evaluated as

$$S_{\theta,l} = \left( \frac{\partial \theta_h}{\partial X} \right)^2 + \left( \frac{\partial \theta_h}{\partial Y} \right)^2, \quad (41)$$

$$S_{\psi,l} = \phi \left\{ 2 \left[ \left( \frac{\partial U_h}{\partial X} \right)^2 + \left( \frac{\partial V_h}{\partial Y} \right)^2 \right] + \left( \frac{\partial U_h}{\partial Y} + \frac{\partial V_h}{\partial X} \right)^2 \right\}, \quad (42)$$

where  $S_{\theta,l}$  and  $S_{\psi,l}$  denote the local entropy generation measures due to heat transfer and fluid friction, respectively. The parameter  $\phi$  is the irreversibility distribution ratio. In its dimensional scaling form, it can be written using a reference viscosity  $\mu_{\text{ref}}$  as

$$\phi = \frac{\mu_{\text{ref}} T_0}{\kappa} \left( \frac{U_0}{\Delta T} \right)^2, \quad (43)$$

where  $T_0 = (T_h + T_c)/2$  is the bulk reference temperature,  $U_0 = \alpha/L$  is the reference velocity scale,  $\Delta T = T_h - T_c$  is the reference temperature difference, and  $\kappa$  is the thermal conductivity. Following [53],  $\phi$  is prescribed as a constant value of  $10^{-4}$  in this study, rather than recomputed from the local apparent viscosity. This keeps the entropy-generation post-processing consistent with the benchmark definition and isolates the effect of rheology through the computed velocity gradients.

The total entropy generation  $S_{\text{total}}$  is obtained by summing the contributions from heat transfer ( $S_{\theta,\text{total}}$ ) and fluid friction ( $S_{\psi,\text{total}}$ ), each evaluated by integrating the respective local rates over the domain  $\Omega$

$$S_{\text{total}} = \int_{\Omega} S_{\theta,l} d\Omega + \int_{\Omega} S_{\psi,l} d\Omega = S_{\theta,\text{total}} + S_{\psi,\text{total}}, \quad (44)$$

where the integrated forms in terms of the discrete FEM fields are

$$S_{\theta,\text{total}} = \int_{\Omega} \left\{ \left[ \frac{\partial}{\partial X} \left( \sum_{k=1}^{N_{\theta}} \theta_k \Phi_k^{\theta} \right) \right]^2 + \left[ \frac{\partial}{\partial Y} \left( \sum_{k=1}^{N_{\theta}} \theta_k \Phi_k^{\theta} \right) \right]^2 \right\} dX dY, \quad (45)$$

$$S_{\psi,\text{total}} = \phi \int_{\Omega} \left\{ 2 \left[ \left( \frac{\partial}{\partial X} \sum_{k=1}^{N_u} U_k \Phi_k^u \right)^2 + \left( \frac{\partial}{\partial Y} \sum_{k=1}^{N_u} V_k \Phi_k^u \right)^2 \right] + \left( \frac{\partial}{\partial Y} \sum_{k=1}^{N_u} U_k \Phi_k^u + \frac{\partial}{\partial X} \sum_{k=1}^{N_u} V_k \Phi_k^u \right)^2 \right\} dX dY. \quad (46)$$

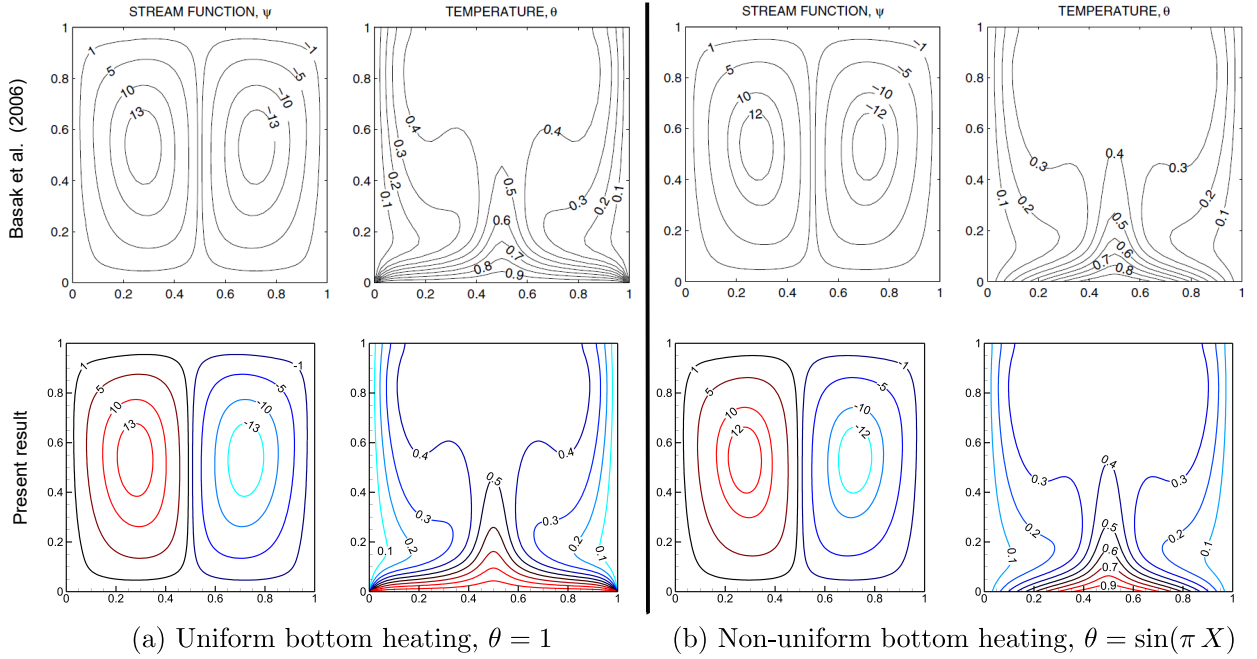


**Figure 2:** Validation of Newtonian natural convection ( $n = 1$ ) in a square cavity with bottom-wall heating: (a) uniform heating ( $\theta = 1$ ) and (b) non-uniform sinusoidal heating ( $\theta = \sin(\pi X)$ ). Stream function and temperature contours from the present FEM simulations (bottom) are compared with the benchmark results of Basak et al. [22] (top) for  $Pr = 0.7$ , and  $Ra = 10^5$ , demonstrating a good agreement in both flow and thermal fields.

All integrals in Eqs. (44)–(46) are evaluated numerically using the numerical framework described in Appendix B.

The relative dominance of heat transfer irreversibility over viscous dissipation is quantified by the average Bejan number  $Be_{av}$ , defined as

$$Be_{av} = \frac{S_{\theta, total}}{S_{\theta, total} + S_{\psi, total}} = \frac{S_{\theta, total}}{S_{total}}. \quad (47)$$

A value of  $Be_{av} > 0.5$  indicates that heat transfer irreversibility dominates, while  $Be_{av} < 0.5$  indicates dominance of fluid friction irreversibility.

## 5. Benchmark Cases

Prior to presenting the main results, the accuracy and reliability of the developed FEM solver are verified through a series of benchmark comparisons covering both Newtonian and non-Newtonian natural convection flows in square and cylindrical geometries, as well as entropy generation predictions. In all validation cases, the dimensionless governing Eqs. (10)–(13) are solved subject to the corresponding benchmark boundary conditions, and the computed quantities are compared against established benchmark solutions from the literature.

### 5.1. Newtonian Natural Convection Flows

As the first benchmark case, Newtonian natural convection ( $n = 1$ ) in a square cavity is examined for two bottom-wall thermal boundary conditions, including uniform and non-uniform sinusoidal heating. In both cases, the vertical side walls are kept at a constant cold temperature and the top wall is adiabatic, and the simulations are carried out at  $Pr = 0.7$  and  $Ra = 10^5$  using a structured grid of  $200 \times 200$  quadrilateral elements. Figure 2 presents the stream function and temperature contours from the present FEM solver alongside the benchmark results of Basak et al. [22]. For uniform heating, the symmetric thermal forcing produces a pair of counter-rotating circulation cells, with pronounced thermal boundary layers developing near the hot bottom and cold side walls, whereas under non-uniform sinusoidal heating the circulation remains symmetric but is driven more strongly by the localized heating at the center of the bottom wall,

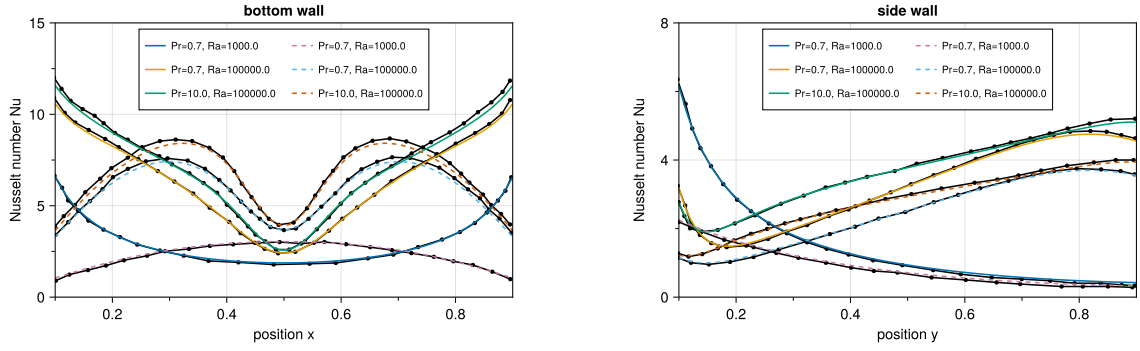


**Figure 3:** Validation of Newtonian natural convection ( $n = 1$ ) in a square cavity with bottom-wall uniform and non-uniform heating. Distributions of the local Nusselt number are shown along (a) the bottom wall and (b) the side wall for  $Pr = 0.7, 10$  and  $Ra = 10^3, 10^5$ . Solid lines represent uniform heating, while dashed lines correspond to non-uniform sinusoidal heating. Present results are compared with benchmark data of Basak et al. [22], shown by symbols.

where the isotherms rise sharply and indicate a strong buoyant plume. A good agreement in both flow patterns and thermal fields for the two heating configurations demonstrates the accuracy and robustness of the present FEM solver.

Figure 3 provides a quantitative validation of the local heat transfer by comparing the local Nusselt number distributions along the bottom and side walls of the square cavity with the benchmark data of Basak et al. [22]. Results are shown for  $Pr = 0.7, 10$  and  $Ra = 10^3, 10^5$  under both uniform and non-uniform sinusoidal bottom-wall heating. Along the bottom wall, uniform heating produces a symmetric profile with peak Nusselt numbers near the side walls, whereas non-uniform heating shifts the peak toward the centrally heated region; increasing  $Ra$  enhances the gradients and raises the local Nusselt levels. Along the side wall, the highest heat transfer occurs near the bottom corner, especially at larger  $Ra$ , due to strong thermal plumes from the heated bottom. The present curves closely match the trends and magnitudes of Basak et al. [22], confirming the solver's accuracy for local heat transfer prediction.

To validate the entropy-generation post-processing framework, a square cavity with a uniformly heated bottom wall is simulated at  $Pr = 0.015$  and  $Ra = 10^3$ , following the configuration of Kaluri and Basak [53]. Figure 4 shows the local entropy generation contours due to heat transfer  $S_{\theta,l}$  and fluid friction  $S_{\psi,l}$  from the present FEM solver together with the reference results of Kaluri and Basak [53]. Heat-transfer entropy production is concentrated on the thermally active walls and corner regions where temperature gradients are largest, whereas viscous entropy production is localized near the cavity corners where velocity gradients are highest. The close agreement in both spatial patterns and relative magnitudes of  $S_{\theta,l}$  and  $S_{\psi,l}$  confirms the accuracy of the proposed entropy post-processing framework.

## 5.2. Non-Newtonian Natural Convection Flows

The next benchmark examines non-Newtonian natural convection of power-law fluids in a square cavity using the present FEM solver, and is compared with the numerical results of Turan et al. [54]. In the square cavity, the vertical walls are held at different temperatures, while the horizontal walls are adiabatic. Both velocity components vanish on all boundaries, enforcing no-slip and impermeable conditions. The simulations are conducted at  $Pr = 10^3$  and  $Ra = 10^4$  for three different power-law indices ( $n = 0.6, 1.0, \text{ and } 1.8$ ). Figure 5 shows the corresponding non-dimensional temperature and stream function contours. For  $n = 0.6$ , the reduced apparent viscosity enhances convection, leading to steep thermal gradients near the vertical walls and stronger circulation. At  $n = 1.0$ , the temperature field is more uniform and a single primary vortex dominates the cavity, as expected for Newtonian flow. For  $n = 1.8$ , the increased viscosity damps motion, yielding weaker circulation and more diffuse, nearly conduction-dominated isotherms. The present FEM predictions closely match those of Turan et al. [54] for all  $n$ , demonstrating that the solver accurately captures power-law rheology effects on non-Newtonian natural convection.

The final benchmark examines non-Newtonian natural convection in a concentric cylindrical annulus, using the present FEM solver and the reference solutions of Matin and Khan [55]. The outer cylinder is kept at a uniform cold temperature ( $T_c$ ), while the inner cylinder is maintained at a uniform hot temperature ( $T_h$ ) with ( $T_c < T_h$ ). The simulations are performed at  $Pr = 100$  and  $Ra = 10^4$  for three power-law indices,  $n = 0.6, 1.0, \text{ and } 1.4$ . Figure 6 illustrates the corresponding streamline and isotherm contours. For  $n = 0.6$ , the reduced apparent viscosity strengthens

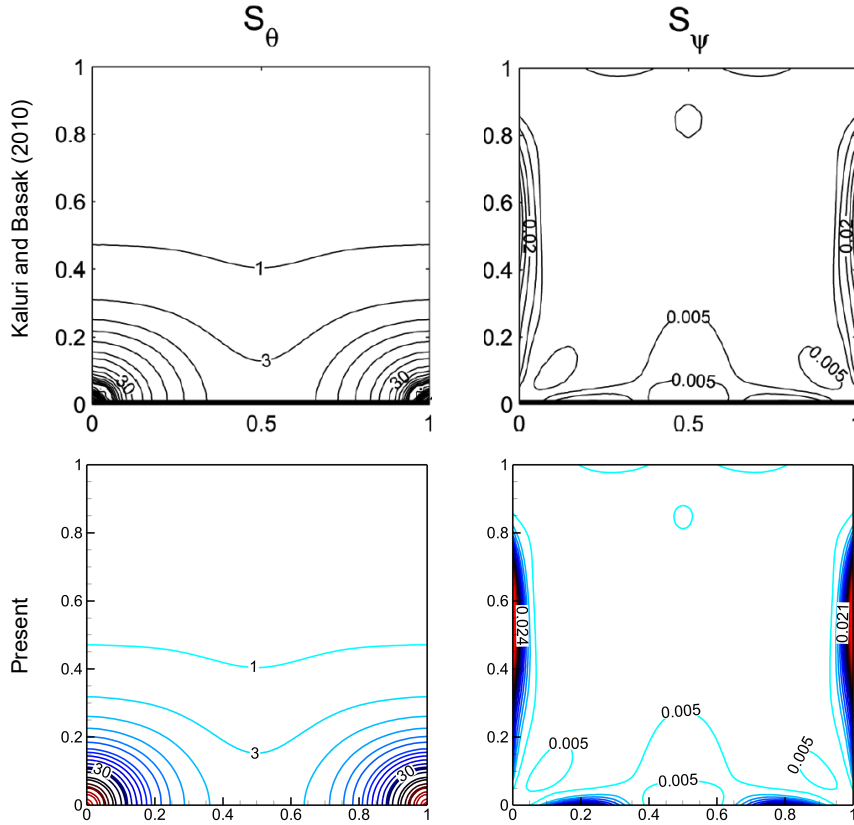


**Figure 4:** Validation of Newtonian natural convection ( $n = 1$ ) in a square cavity with uniform heated bottom wall. Local entropy generation contours due to heat transfer  $S_{\theta,l}$  and fluid friction  $S_{\psi,l}$  are shown at  $Pr = 0.015$  and  $Ra = 10^3$ . Present FEM results are compared against the numerical data of Kaluri and Basak [53].

convection near the heated inner cylinder, generating compact vortices and strongly distorted isotherms that indicate vigorous radial heat transport. At  $n = 1.0$ , the flow becomes more symmetric and the isotherms are only moderately displaced from the purely conductive pattern, typical of Newtonian convection. For  $n = 1.4$ , the higher apparent viscosity substantially damps circulation, and the isotherms become nearly concentric, signaling conduction-dominated transport. The present FEM predictions match those of Matin and Khan [55] for both velocity and temperature fields across all three rheological regimes, demonstrating the robustness and accuracy of the proposed framework for non-Newtonian natural convection in cylindrical geometries.

## 6. Numerical results and discussion

This section presents the numerical results obtained using the FEM solver for the square cavity and concentric cylindrical annulus configurations. The effects of thermal boundary conditions and power-law rheology on the flow structure, heat transfer, and entropy generation are examined systematically. Particular attention is given to the influence of the Rayleigh number and the power-law index on the transport characteristics in both geometries. The simulations are performed at  $Pr = 100$ ,  $Ra = 10^4$ , and for  $n = 0.6, 1.0, \text{ and } 1.4$ . Flow behavior is characterized using streamlines and heatlines, heat-transfer performance is evaluated through local and average Nusselt numbers, and thermodynamic irreversibility is assessed from entropy generation due to heat transfer and viscous dissipation.

### 6.1. Grid independence study

A mesh-independence study is conducted for both geometries to ensure grid-independent solutions. Three mesh resolutions are examined, illustrated in Fig. 7: structured quadrilateral meshes are used for the square cavity, whereas unstructured meshes with radial refinement are employed for the concentric cylindrical annulus. The average Nusselt

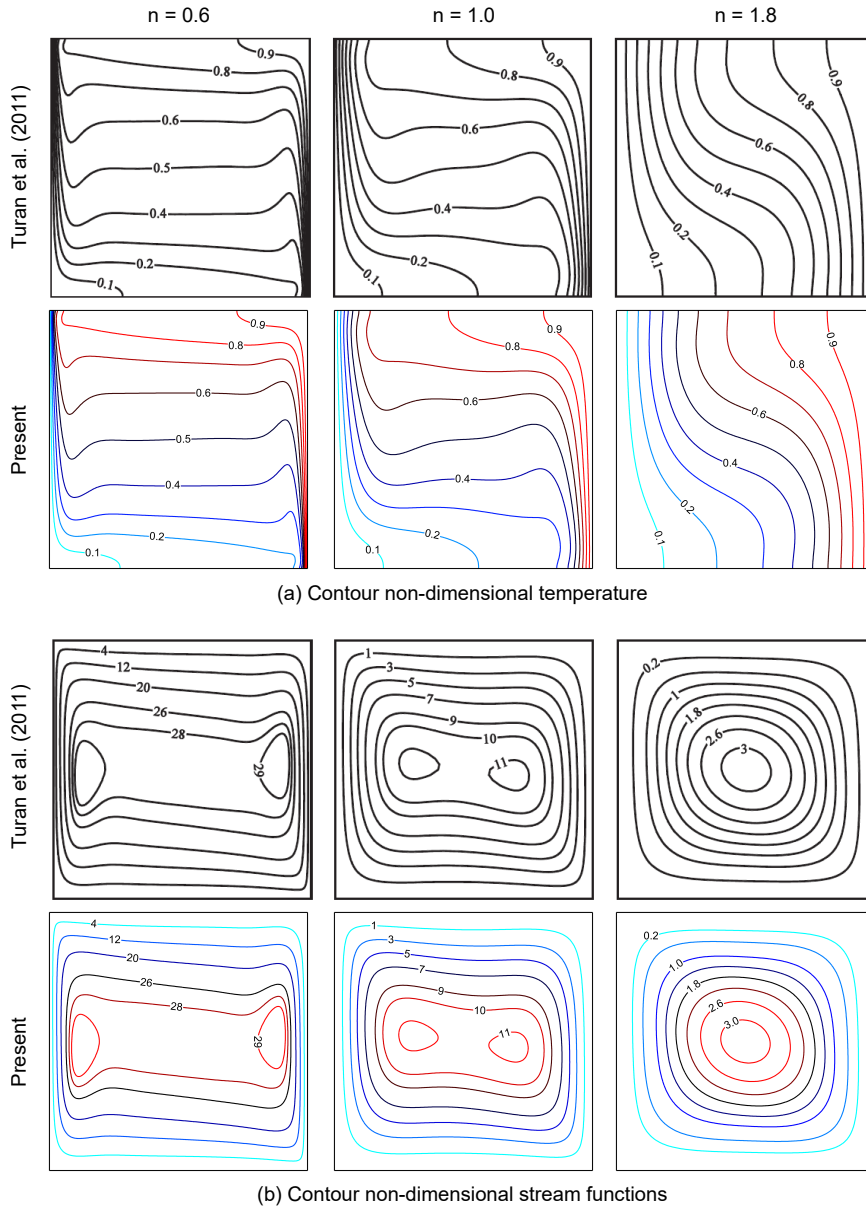


**Figure 5:** Validation of non-Newtonian natural convection in a differentially heated square cavity for  $Pr = 10^3$ ,  $Ra = 10^4$ , and power-law indices  $n = 0.6, 1.0$ , and  $1.8$ : comparison of non-dimensional (a) temperature and (b) stream function contours between Turan et al. [54] and the present FEM solver.

number at the heated wall, maximum local entropy generation due to heat transfer ( $S_{\theta, \max}$ ), and fluid friction ( $S_{\psi, \max}$ ) are monitored across all mesh levels (Tables 1 and 2). For the square cavity, all three quantities exhibit negligible variation beyond Mesh 3 (Table 1). A consistent trend is observed for the concentric cylinder annulus, where  $Nu_{\text{inner}}$ ,  $S_{\theta, \max}$ , and  $S_{\psi, \max}$  stabilize from Mesh 3 onward (Table 2). Accordingly, Mesh 3 is adopted for all subsequent simulations, providing an optimal balance between computational efficiency and solution accuracy.

## 6.2. Square cavity configuration

This subsection examines the effects of the power-law index  $n$  and thermal boundary conditions on non-Newtonian natural convection in the square cavity, considering both uniform and non-uniform sinusoidal bottom-wall heating at  $Pr = 100$  and  $Ra = 10^4$ .

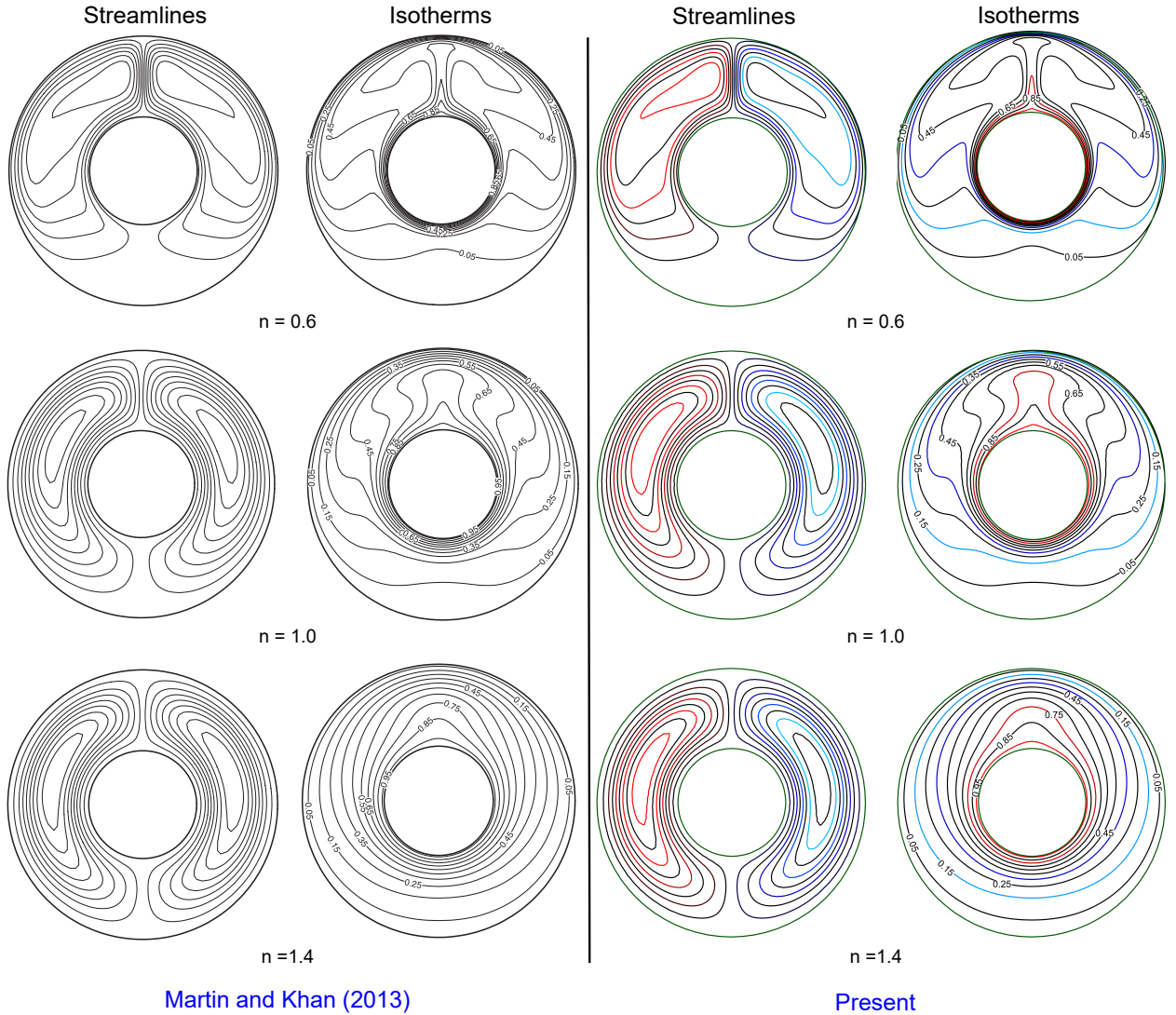


**Figure 6:** Validation of non-Newtonian natural convection in a concentric cylindrical annulus for  $Pr = 100$ ,  $Ra = 10^4$ , and power-law indices  $n = 0.6$ ,  $1.0$ , and  $n = 1.4$ . Comparison of streamline and isotherm contours between Martin and Khan [55] and the present FEM results.

### 6.2.1. Flow structure and thermal fields

Figure 8 illustrates the isotherms  $\theta$ , streamlines  $\psi$ , and heatlines  $\Pi$  for  $n = 0.6$ ,  $1.0$ , and  $1.4$  in the square cavity with uniform bottom-wall heating ( $\theta = 1$ ). For the shear-thinning fluid ( $n = 0.6$ ), the reduced apparent viscosity enhances buoyancy-driven circulation, producing two strong counter-rotating vortices that occupy the lower portion of the cavity, while the isotherms exhibit steep thermal gradients near the heated bottom wall and a thermally stratified core, indicating vigorous convective transport. At  $n = 1.0$ , the flow transitions to a more symmetric pattern with expanded vortex structures and moderately distorted isotherms, consistent with classical Newtonian natural convection. For the shear-thickening fluid ( $n = 1.4$ ), the increased apparent viscosity suppresses fluid motion considerably, yielding weaker and more diffuse streamlines and nearly parallel isotherms that reflect a conduction-dominated thermal field. The heatlines confirm these trends: concentrated and curved  $\Pi$ -contours for  $n = 0.6$  indicate strong convective heat flux from the bottom wall, which progressively weakens and becomes more uniform as  $n$  increases toward shear-thickening behavior.

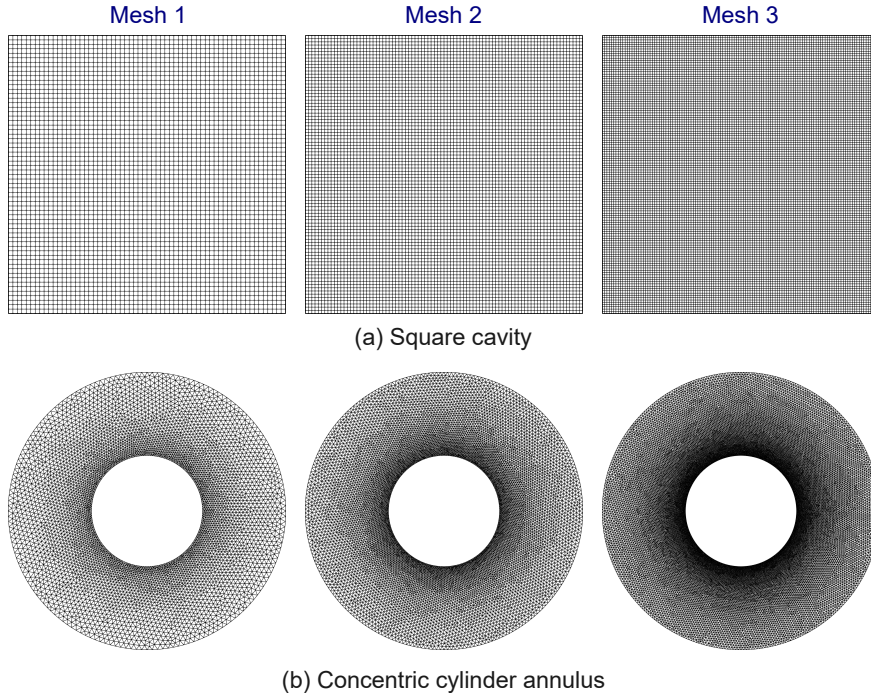


**Figure 7:** Mesh convergence study for the two computational domains: (a) structured quadrilateral meshes (Mesh 1–3) for the square cavity, and (b) unstructured triangular meshes (Mesh 1–3) for the concentric cylindrical annulus. Three progressively refined mesh resolutions are compared to assess grid independence and ensure numerical accuracy.

**Table 1**

Grid independence study for the square cavity: variation of the average Nusselt number at the bottom wall ( $\overline{Nu}_{bot}$ ), maximum local entropy generation due to heat transfer ( $S_{\theta,max}$ ), and fluid friction ( $S_{\psi,max}$ ) with mesh refinement.

id	$n_{elems}$	$n_{nodes}$	$\overline{Nu}_{bot}$	$S_{\theta,max}$	$S_{\psi,max}$
1	3844	3969	6.6704	104.3720	2406.6836
2	7396	7569	6.6460	103.5721	2450.5564
3	14884	15129	6.6312	103.0823	2475.2736
4	29584	29929	6.6232	102.8219	2487.4909
5	59536	60025	6.6189	102.6823	2493.9131

**Table 2**

Grid independence study for the concentric cylinder annulus: variation of the average Nusselt number at the inner wall ( $Nu_{inner}$ ), maximum local entropy generation due to heat transfer ( $S_{\theta,max}$ ), and fluid friction ( $S_{\psi,max}$ ) with mesh refinement.

ID	$n_{elems}$	$n_{nodes}$	$Nu_{inner\ avg}$	$S_{\theta,max}$	$S_{\psi,max}$
1	10254	5306	4.0284	55.6149	1988.3033
2	19976	10240	4.0224	56.0836	1980.8299
3	40012	20363	4.0215	56.2028	2035.7779
4	79434	40221	4.0221	56.1087	1726.6153
5	158098	79761	4.0218	56.1371	1720.5476

Figure 9 presents the isotherms  $\theta$ , streamlines  $\psi$ , and heatlines  $\Pi$  for  $n = 0.6, 1.0$ , and  $1.4$  under non-uniform sinusoidal bottom-wall heating ( $\theta = \sin(\pi X)$ ). Compared to the uniform heating case (Fig. 8), the sinusoidal boundary condition introduces a spatially localized thermal forcing at the cavity center, which breaks the symmetric thermal stratification and generates a distinct central buoyant plume visible in the isotherms for all values of  $n$ . For  $n = 0.6$ , the shear-thinning effect amplifies this plume-driven convection, producing tightly packed streamlines and strongly

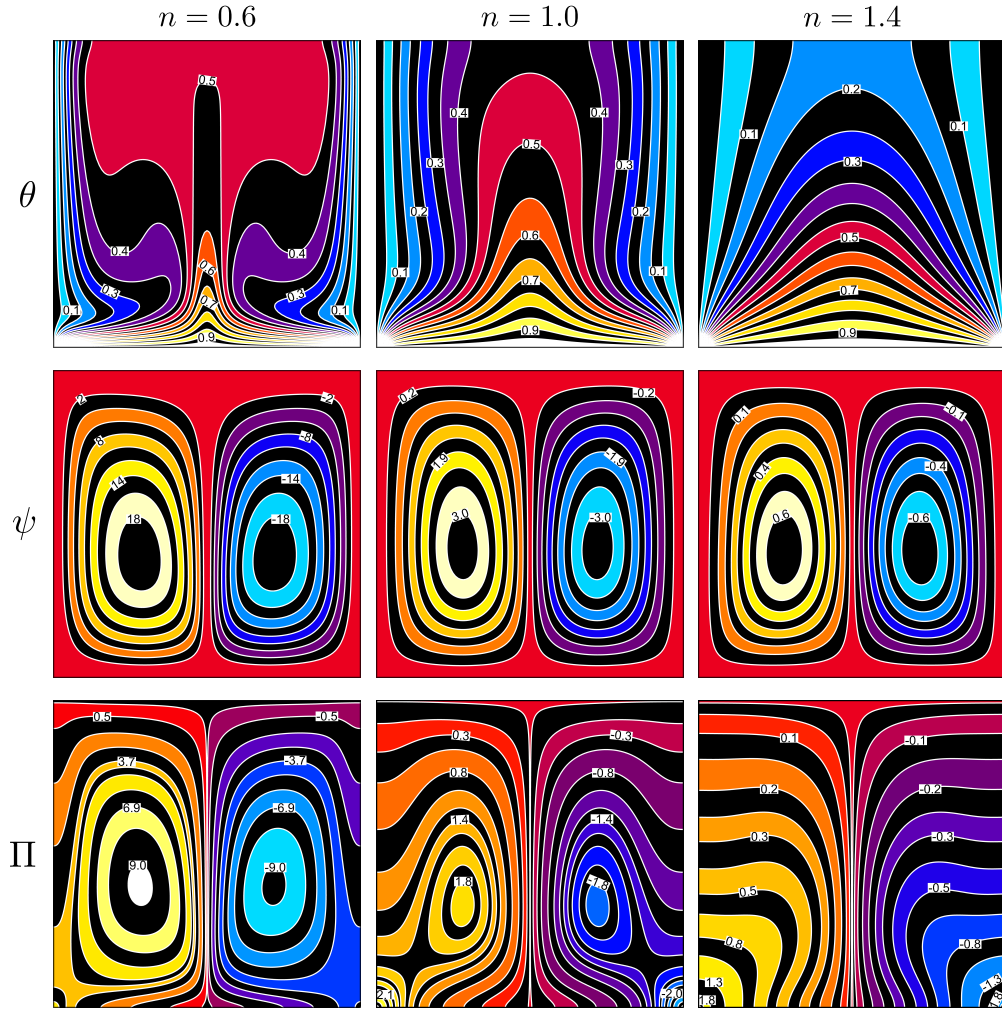


**Figure 8:** Isotherms  $\theta$  (top), streamlines  $\psi$  (middle), and heatlines  $\Pi$  (bottom) of power-law index  $n = 0.6, 1.0,$  and  $1.4$  in a square cavity with uniform bottom-wall heating ( $\theta = 1$ ).

distorted isotherms concentrated near the bottom center, whereas the heatlines indicate intense convective heat flux directed upward from the peak-heated region. At  $n = 1.0$ , the flow retains two counter-rotating vortices but with reduced intensity compared to the shear-thinning case, and the isotherms show moderate thermal gradients consistent with Newtonian behavior under localized heating. For  $n = 1.4$ , viscous damping significantly weakens circulation, and the isotherms approach a near-conductive distribution; however, unlike the uniform heating case, a residual central plume persists due to the concentrated sinusoidal heat input, and the heatlines become increasingly diffuse, reflecting the dominance of conduction over convection in the shear-thickening regime.

### 6.2.2. Nusselt number and heat transfer

Figure 10 compares the local Nusselt number distributions along the bottom wall for  $n = 0.6, 1.0,$  and  $1.4$  under uniform and non-uniform sinusoidal heating. Under uniform heating, the local  $Nu$  exhibits a symmetric U-shaped profile, with peak values concentrated near the side walls due to intense thermal boundary layer development driven by the cold vertical walls, and a minimum at the cavity center where convective mixing is relatively weak. In contrast, non-uniform sinusoidal heating ( $\theta = \sin(\pi X)$ ) reverses this trend, producing an M-shaped profile with two local maxima near  $X = 0.25$  and  $X = 0.75$  and a reduced value at the center, consistent with the localized buoyant plume generated by the sinusoidal temperature peak at  $X = 0.5$ . In both cases, the shear-thinning fluid ( $n = 0.6$ ) yields

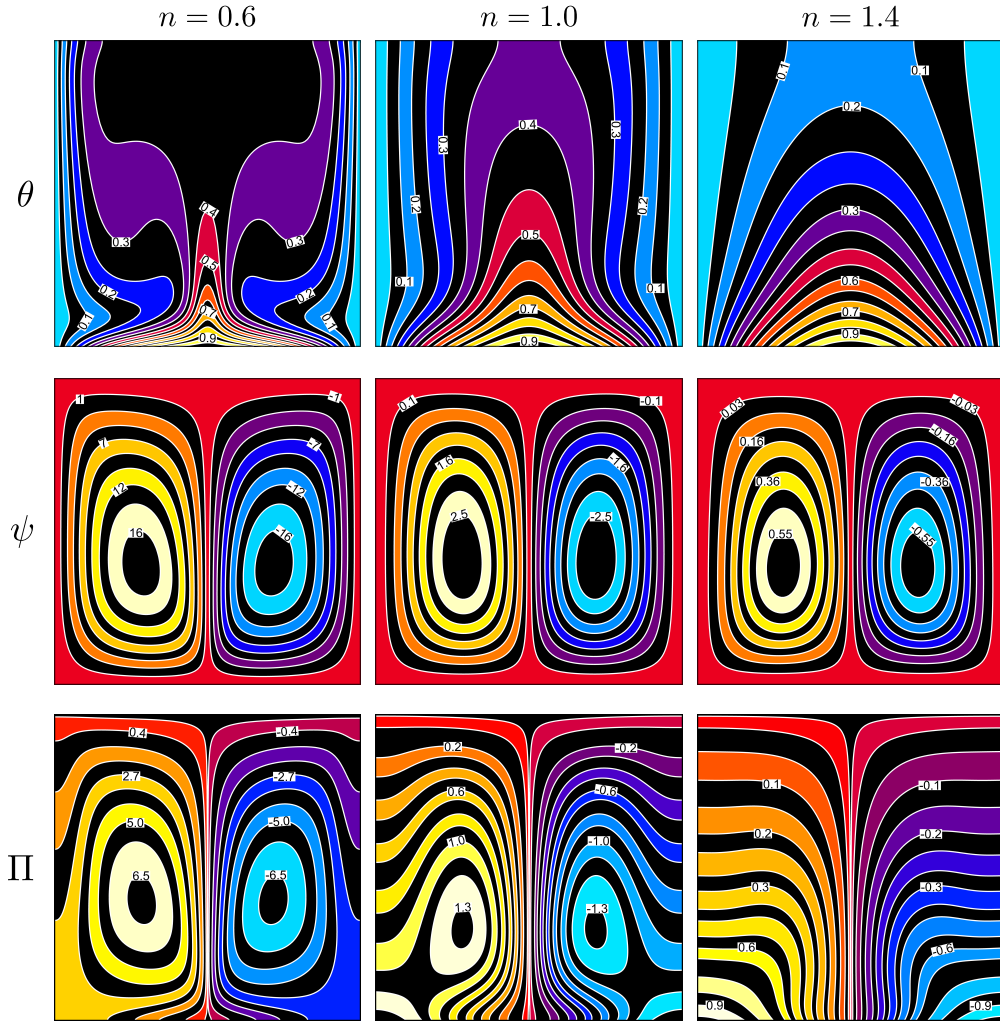


**Figure 9:** Isotherms  $\theta$  (top), streamlines  $\psi$  (middle), and heatlines  $\Pi$  (bottom) of power-law index  $n = 0.6, 1.0,$  and  $1.4$  in a square cavity with non-uniform bottom-wall heating ( $\theta = \sin(\pi X)$ ).

the highest  $Nu$  values owing to its reduced apparent viscosity, which enhances convective transport, while the shear-thickening fluid ( $n = 1.4$ ) produces the lowest heat transfer rates across the entire wall due to viscous suppression of fluid motion. Notably, the difference in  $Nu$  between rheological regimes is more pronounced under non-uniform heating, suggesting that sinusoidal thermal forcing amplifies the sensitivity of heat transfer to power-law rheology compared to the uniform heating case.

Figure 11 presents the local Nusselt number distributions along the left (cold) side wall of the square cavity for  $n = 0.6, 1.0,$  and  $1.4$  under uniform and non-uniform sinusoidal bottom-wall heating ( $\theta = \sin(\pi X)$ ). Under uniform heating, the local  $Nu$  along the side wall exhibits its maximum near the bottom corner, where the rising thermal plume from the uniformly heated bottom wall impinges directly on the cold vertical surface, generating steep thermal gradients; the heat transfer rate decays monotonically toward the adiabatic top wall as the thermal boundary layer thickens with increasing height. Under non-uniform sinusoidal heating, the side wall  $Nu$  distribution retains a similar decreasing trend from bottom to top but with a notably lower peak value compared to the uniform case, since the sinusoidal heating concentrates thermal energy at the cavity center rather than uniformly energizing the bottom wall, thereby reducing the thermal gradient at the bottom corner of the side wall. Across both heating conditions, the shear-thinning fluid ( $n = 0.6$ ) produces the highest local  $Nu$  values along the side wall, driven by its enhanced convective circulation, while the shear-thickening fluid ( $n = 1.4$ ) yields the lowest heat transfer rates due to viscous suppression; however, the rheological spread between the three  $n$ -values is more pronounced under uniform heating, confirming that

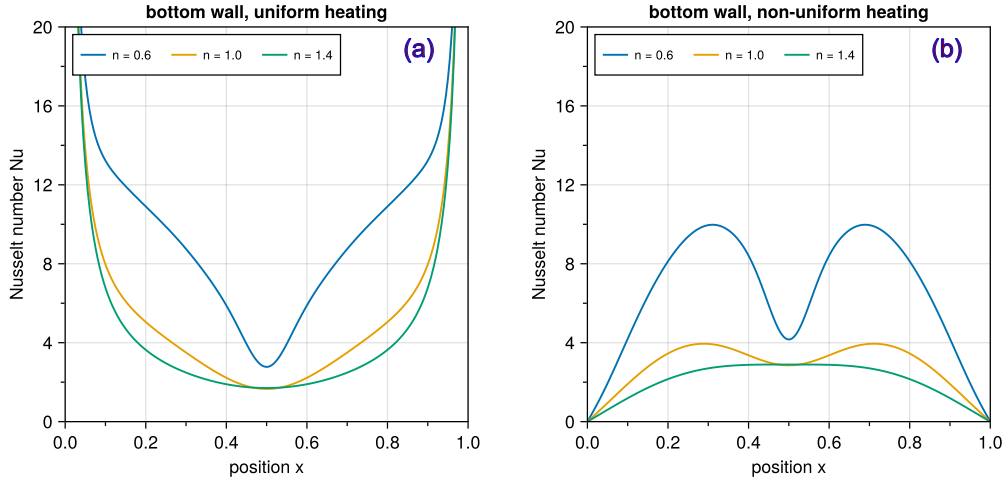


**Figure 10:** Local Nusselt number distributions along the bottom wall of the square cavity for power-law indices  $n = 0.6$ , 1.0, and 1.4 under (a) uniform heating ( $\theta = 1$ ) and (b) non-uniform sinusoidal heating ( $\theta = \sin(\pi X)$ ).

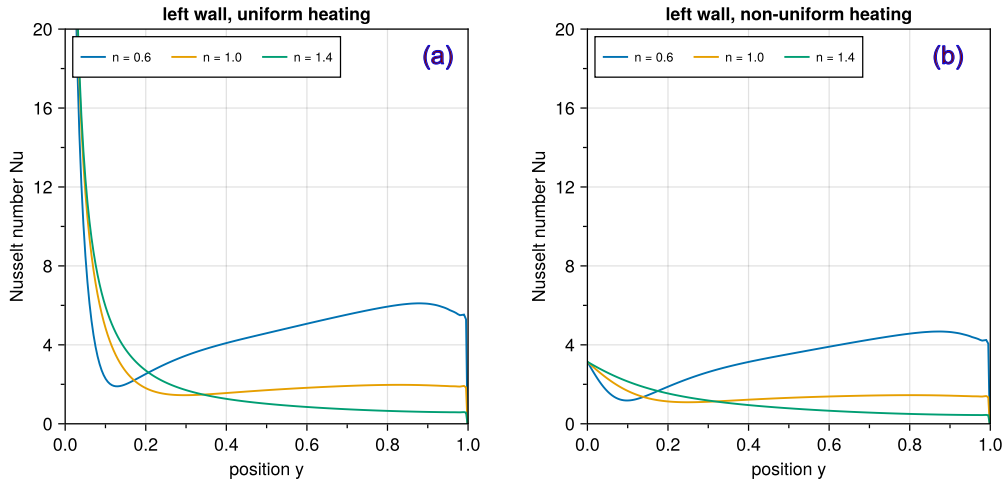


**Figure 11:** Local Nusselt number distributions along the left wall of the square cavity for power-law indices  $n = 0.6$ , 1.0, and 1.4 under (a) uniform heating ( $\theta = 1$ ) and (b) non-uniform sinusoidal heating ( $\theta = \sin(\pi X)$ ).

uniform thermal loading engages the full convective capacity of the cavity more effectively than localized sinusoidal forcing.

### 6.2.3. Entropy generation and Bejan number

Figure 12 presents the contours of local entropy generation due to heat transfer  $S_\theta$  and fluid friction  $S_\psi$  for  $n = 0.6$ , 1.0, and 1.4 under uniform bottom-wall heating. The  $S_\theta$  contours are most concentrated near the cold vertical side walls and along the heated bottom wall, regions that correspond directly to the steep isotherm gradients observed in Fig. 8, where the thermal boundary layers are thinnest and the temperature difference between fluid and wall is greatest. For  $n = 0.6$ , the shear-thinning fluid exhibits the highest  $S_\theta$  magnitudes, consistent with the strongly distorted isotherms and vigorous counter-rotating vortices seen in the streamline contours of Fig. 8, which intensify thermal gradients at the walls and thereby amplify heat transfer irreversibility. As  $n$  increases to 1.4, the weakened circulation evident in the streamlines leads to a more diffuse  $S_\theta$  distribution and reduced peak magnitudes, reflecting the conduction-dominated thermal field. The  $S_\psi$  contours are highly localized near the cavity corners and the bottom wall, where the tightly packed streamlines in Fig. 8 indicate peak velocity gradients; these magnitudes decrease progressively with increasing  $n$ , as shear-thickening rheology suppresses fluid motion and reduces viscous dissipation. Hence,  $S_\theta$  dominates over

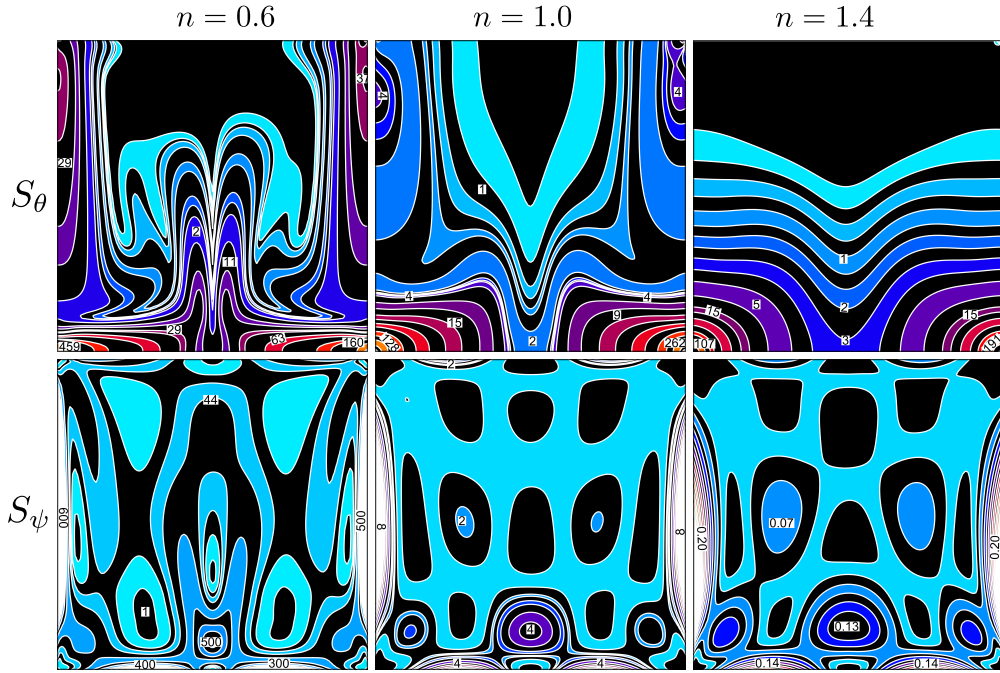


**Figure 12:** Contours of local entropy generation due to heat transfer  $S_\theta$  (top) and fluid friction  $S_\psi$  (bottom) for power-law indices  $n = 0.6, 1.0,$  and  $1.4$  in the square cavity with uniform bottom-wall heating ( $\theta = 1$ ).

$S_\psi$  across all rheological regimes, confirming that heat transfer irreversibility is the primary source of thermodynamic inefficiency in buoyancy-driven power-law fluid convection at the considered Ra.

Figure 13 presents the contours of local entropy generation due to heat transfer  $S_\theta$  and fluid friction  $S_\psi$  for  $n = 0.6, 1.0,$  and  $1.4$  under non-uniform sinusoidal bottom-wall heating ( $\theta = \sin(\pi X)$ ). In contrast to the uniform heating case (Fig. 12), the  $S_\theta$  contours are no longer uniformly distributed along the bottom wall but instead exhibit a spatially concentrated pattern directly above the central peak of the sinusoidal temperature profile, consistent with the localized buoyant plume and sharply rising isotherms observed at the cavity center in Fig. 9. For  $n = 0.6$ , the reduced apparent viscosity intensifies the central plume-driven convection, producing the highest  $S_\theta$  magnitudes among all rheological cases, with peak irreversibility localized in the plume column where thermal gradients are steepest; this is corroborated by the tightly clustered isotherms and strong upward convective motion seen in the streamlines of Fig. 9. As  $n$  increases to  $1.4$ , the weakened circulation suppresses the central plume, leading to a considerably more diffuse  $S_\theta$  field with significantly reduced peak values compared to both the shear-thinning case and the corresponding uniform heating scenario in Fig. 12, reflecting the dominance of conduction in the shear-thickening regime. The  $S_\psi$  contours remain localized near the cavity corners and bottom wall edges across all  $n$ -values, where the streamlines in Fig. 9 indicate the highest velocity gradients; however, the  $S_\psi$  magnitudes under non-uniform heating are notably lower than those in the uniform heating case, since the sinusoidal forcing concentrates fluid motion near the cavity center rather than energizing the full bottom wall, thereby reducing overall fluid friction.

The total entropy generation due to heat transfer ( $S_{\theta,\text{total}}$ ), fluid friction ( $S_{\psi,\text{total}}$ ), combined total entropy generation ( $S_{\text{total}}$ ), and average Bejan number ( $\text{Be}_{\text{av}}$ ) for both heating configurations are quantified in Table 3. Under uniform heating, the shear-thinning fluid ( $n = 0.6$ ) yields the highest  $S_{\text{total}} = 101.39$ , predominantly driven by viscous dissipation ( $S_{\psi,\text{total}} = 87.77$ ), consistent with the intense and widespread  $S_\psi$  contours observed near the cavity corners and bottom wall in Fig. 12; the corresponding low  $\text{Be}_{\text{av}} = 0.134$  confirms that fluid friction irreversibility dominates overwhelmingly compared to heat transfer irreversibility for shear-thinning fluids under uniform heating. As  $n$  increases to  $1.6$ ,  $S_{\psi,\text{total}}$  drops sharply to  $0.050$ , reducing  $S_{\text{total}}$  to  $8.57$ , while  $\text{Be}_{\text{av}}$  approaches unity ( $0.994$ ), indicating that heat transfer irreversibility becomes almost exclusively dominant - corroborated by the diffuse and weak  $S_\psi$  contours and relatively persistent  $S_\theta$  patterns seen in Fig. 10 for  $n = 1.4$ . Under non-uniform sinusoidal heating, the same rheological trend holds but with markedly reduced absolute values of both  $S_{\theta,\text{total}}$  and  $S_{\psi,\text{total}}$  across all  $n$ , reflecting the spatially localized nature of the sinusoidal thermal forcing, which concentrates entropy production near the cavity center rather

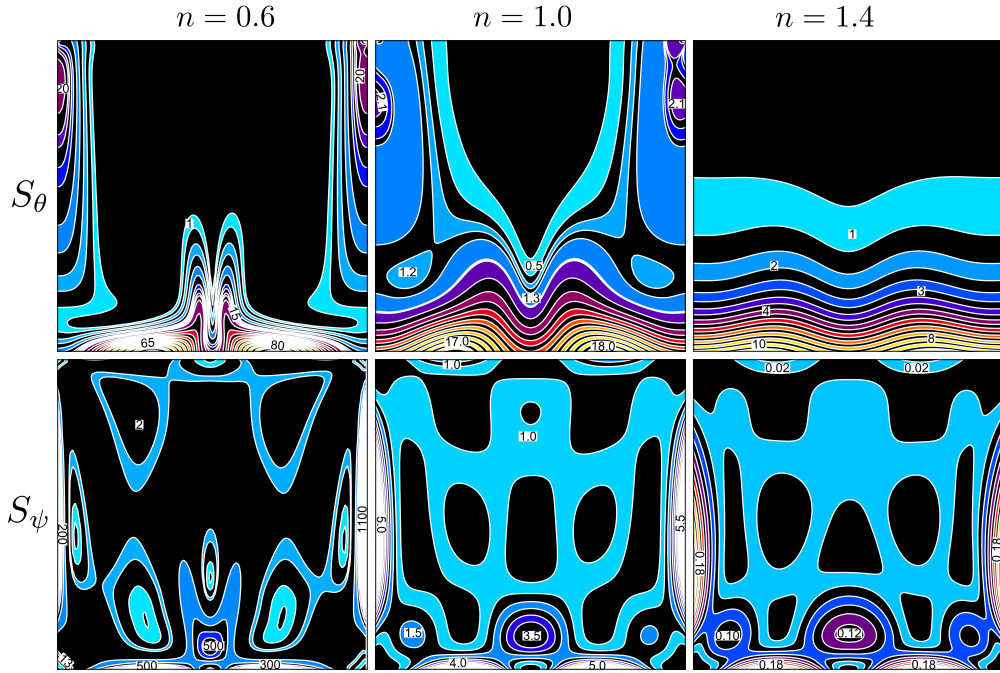


**Figure 13:** Contours of local entropy generation due to heat transfer  $S_\theta$  (top) and fluid friction  $S_\psi$  (bottom) for power-law indices  $n = 0.6, 1.0,$  and  $1.4$  in the square cavity with non-uniform bottom-wall heating ( $\theta = \sin(\pi X)$ ).

**Table 3**

Total entropy generation due to heat transfer ( $S_{\theta,\text{total}}$ ), fluid friction ( $S_{\psi,\text{total}}$ ), combined total entropy generation ( $S_{\text{total}}$ ), and average Bejan number ( $Be_{\text{av}}$ ) for power-law indices  $n = 0.6, 1.0,$  and  $1.6$  in the square cavity under uniform and non-uniform bottom-wall heating.

Uniform heating bottom wall				
$n$	$S_{\theta,\text{total}}$	$S_{\psi,\text{total}}$	$S_{\text{total}}$	$Be_{\text{av}}$
0.6	13.6196183	87.76998397	101.3896023	0.134329537
1.0	9.332793581	1.265645494	10.59843907	0.880581897
1.6	8.519506667	0.050049404	8.56955607	0.994159627

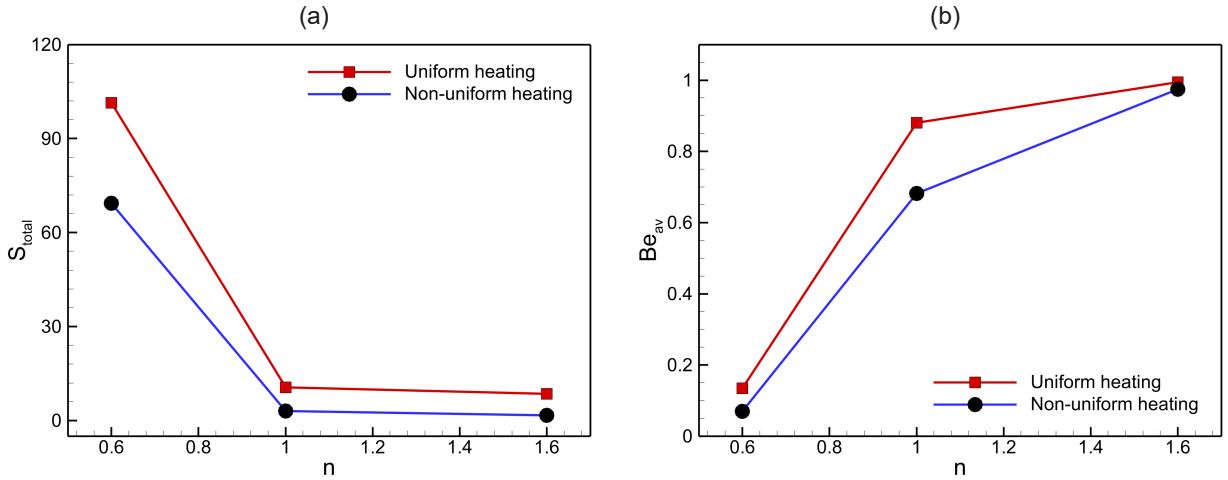
  

Non-uniform heating bottom wall				
$n$	$S_{\theta,\text{total}}$	$S_{\psi,\text{total}}$	$S_{\text{total}}$	$Be_{\text{av}}$
0.6	4.847500594	64.45955406	69.30705466	0.06942383
1.0	2.086104613	0.972145055	3.058249669	0.682123711
1.6	1.600679168	0.041713492	1.64239266	0.974601998

than energizing the full bottom wall, as confirmed by the centrally confined  $S_\theta$  and  $S_\psi$  contours in Fig. 13. Notably, for  $n = 0.6$  under non-uniform heating,  $S_{\text{total}}$  decreases from 101.39 to 69.31, with  $Be_{\text{av}}$  falling further to 0.069, indicating an even stronger dominance of viscous dissipation compared to the uniform heating case. For  $n = 1.0$  and  $n = 1.6$ ,  $Be_{\text{av}}$  increases toward unity under both heating conditions, as further illustrated by the monotonic decrease in  $S_{\text{total}}$  and corresponding rise in  $Be_{\text{av}}$  with increasing  $n$  in Fig. 14.

### 6.3. Concentric cylindrical annulus configuration

This subsection examines the effects of the power-law index  $n$  and thermal boundary conditions on natural convection in the concentric cylindrical annulus, considering both uniform and non-uniform sinusoidal inner-wall heating at  $Pr = 100$  and  $Ra = 10^4$ .



**Figure 14:** Variation of (a) total entropy generation  $S_{\text{total}}$  and (b) average Bejan number  $Be_{\text{av}}$  with power-law index  $n$  in the square cavity under uniform ( $\theta = 1$ ) and non-uniform ( $\theta = \sin(\pi X)$ ) bottom-wall heating.

### 6.3.1. Flow structure and thermal fields

Figure 15 illustrates the isotherms  $\theta$ , streamlines  $\psi$ , and heatlines  $\Pi$  for  $n = 0.6, 1.0$ , and  $1.4$  in the concentric cylindrical annulus under uniform inner-wall heating ( $\theta = 1$ ). For  $n = 0.6$ , pronounced temperature gradients develop near the heated inner wall, and the isotherms are strongly distorted, reflecting vigorous buoyancy-driven convection. The flow is characterized by intense, asymmetric counter-rotating vortices with a maximum stream function magnitude of  $|\psi|_{\text{max}} = 41.25$ , which significantly enhances convective heat transport. Correspondingly, the heatlines indicate strong advective heat transfer, with a high heat function magnitude ( $\Pi_{\text{max}} = 24.17$ ) concentrated near the inner wall and vortex cores, where steep thermal and velocity gradients prevail. As the fluid transitions to Newtonian behavior ( $n = 1.0$ ), the flow structure becomes more symmetric and the isotherms gradually align, indicating a reduction in convective intensity. The circulation strength decreases substantially ( $|\psi|_{\text{max}} = 12.47$ ), accompanied by a marked reduction in heat transport ( $\Pi_{\text{max}} = 6.97$ ), signifying a shift toward moderately convection-dominated heat transfer. For  $n = 1.4$ , the increased effective viscosity suppresses fluid motion, resulting in weak circulation ( $|\psi|_{\text{max}} = 4.06$ ) and nearly concentric isotherms, indicative of conduction-dominated transport. The corresponding heatlines exhibit minimal distortion, and the reduced heat function magnitude ( $\Pi_{\text{max}} = 2.16$ ) reflects significantly lower thermal transport and irreversibility.

Figure 16 presents the isotherms  $\theta$ , streamlines  $\psi$ , and heatlines  $\Pi$  for  $n = 0.6, 1.0$ , and  $1.4$  in the concentric cylindrical annulus under non-uniform sinusoidal inner-wall heating ( $\theta = 0.5(1 + \sin \varphi)$ ). Compared to the uniform heating case (Fig. 15), the spatially varying thermal boundary condition introduces pronounced azimuthal asymmetry in both the flow and thermal fields across all rheological regimes. For  $n = 0.6$ , the isotherms are strongly distorted and concentrated in the upper annular region where heating is maximum, driving asymmetric counter-rotating vortices with reduced circulation strength ( $|\psi|_{\text{max}} = 32.41$ ) compared to uniform heating ( $|\psi|_{\text{max}} = 41.25$ ); the heatlines confirm that convective heat transport is confined to preferred angular regions, yielding a lower heat function magnitude ( $\Pi_{\text{max}} = 14.81$ ). At  $n = 1.0$ , the flow weakens further ( $|\psi|_{\text{max}} = 9.64$ ) while retaining the azimuthal asymmetry imposed by the sinusoidal profile, and heat transport becomes more spatially confined ( $\Pi_{\text{max}} = 6.97$ ) relative to the uniform heating configuration. For  $n = 1.4$ , the increased apparent viscosity strongly suppresses fluid motion ( $|\psi|_{\text{max}} = 3.39$ ), producing nearly stratified isotherms and a significantly diminished heat function ( $\Pi_{\text{max}} = 1.90$ ), indicating a conduction-dominated thermal field.

### 6.3.2. Nusselt number and heat transfer

Figure 17 presents the local Nusselt number distributions along the inner wall of the concentric cylindrical annulus for  $n = 0.6, 1.0$ , and  $1.4$  under uniform and non-uniform sinusoidal inner-wall heating. In both cases, the shear-thinning fluid ( $n = 0.6$ ) yields the highest  $Nu$  values owing to its reduced apparent viscosity, which intensifies buoyancy-driven circulation and thins the thermal boundary layer at the heated wall, while the shear-thickening fluid ( $n = 1.4$ ) produces the lowest values due to viscous suppression of convective transport. Under uniform heating, the  $Nu$  distribution

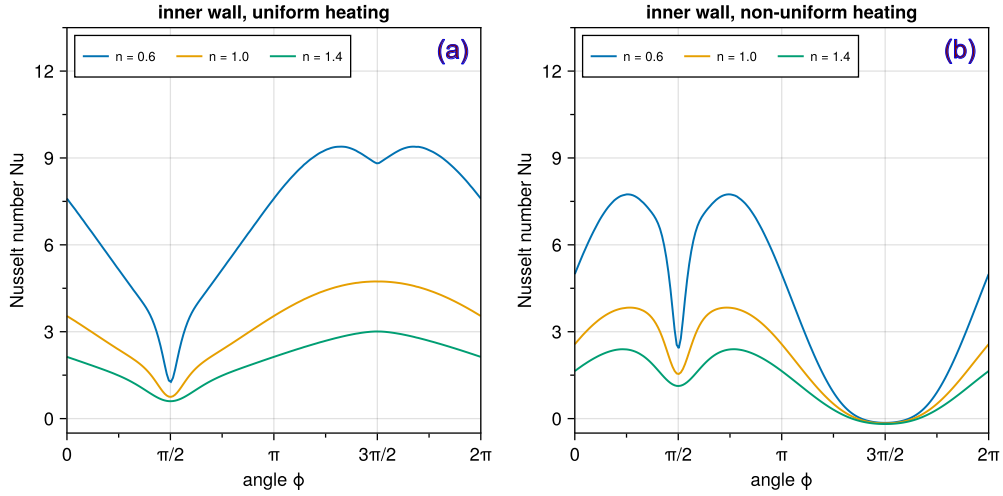


**Figure 15:** Isotherms  $\theta$  (top), streamlines  $\psi$  (middle), and heatlines  $\Pi$  (bottom) for power-law indices  $n = 0.6$ ,  $1.0$ , and  $1.4$  in the concentric cylindrical annulus with uniform inner-wall heating ( $\theta = 1$ ).

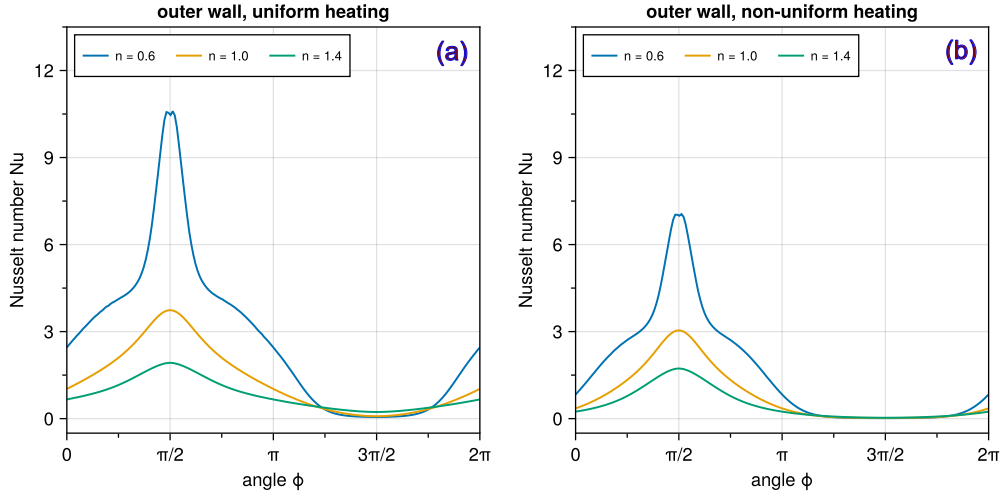
exhibits an asymmetric profile with elevated values over the upper annular region, where buoyancy-enhanced wall-normal heat transfer is strongest, and a pronounced minimum near  $\varphi = \pi/2$ , where local flow reorientation weakens thermal gradients at the wall. Under non-uniform sinusoidal heating, the  $Nu$  distribution develops a more structured angular variation with distinct peaks and troughs that follow the imposed thermal loading; the minimum near  $\varphi \approx 3\pi/2$  corresponds to the weakly heated region where buoyancy production is smallest, while peak values in the upper sectors mark zones of stronger plume formation and more effective heat removal. Compared to uniform heating, non-uniform sinusoidal forcing redistributes heat transfer intensity into localized angular regions, with this localization most pronounced for  $n = 0.6$ , where the lower effective viscosity amplifies plume strength and angular non-uniformity in the thermal boundary layer.

Figure 18 presents the local Nusselt number distributions along the outer wall of the concentric cylindrical annulus for  $n = 0.6$ ,  $1.0$ , and  $1.4$  under uniform and non-uniform sinusoidal inner-wall heating. In both cases, the  $Nu$  distribution exhibits a sharp peak near  $\varphi = \pi/2$ , corresponding to the uppermost point of the annulus where the buoyant thermal plume rising from the heated inner cylinder impinges most directly on the cold outer wall, generating the steepest wall-normal temperature gradients. The shear-thinning fluid ( $n = 0.6$ ) produces the highest peak  $Nu$  value ( $Nu_{max} \approx 10.5$  under uniform heating), as the reduced apparent viscosity intensifies plume-driven convection and enhances heat delivery to the outer wall, while the shear-thickening fluid ( $n = 1.4$ ) yields a nearly flat, low-amplitude profile indicative of conduction-dominated transport with minimal convective contribution. Under non-uniform sinusoidal heating, the





**Figure 17:** Local Nusselt number distributions along the inner wall of the concentric cylindrical annulus for power-law indices  $n = 0.6, 1.0,$  and  $1.4$  under (a) uniform heating ( $\theta = 1$ ) and (b) non-uniform sinusoidal heating ( $\theta = 0.5(1 + \sin \varphi)$ ).



**Figure 18:** Local Nusselt number distributions along the outer wall of the concentric cylindrical annulus for power-law indices  $n = 0.6, 1.0,$  and  $1.4$  under (a) uniform heating ( $\theta = 1$ ) and (b) non-uniform sinusoidal heating ( $\theta = 0.5(1 + \sin \varphi)$ ).

throughout the domain, consistent with the weak velocity gradients and conduction-dominated thermal field observed in the streamlines and isotherms of Fig. 15.

Figure 20 presents the contours of local entropy generation due to heat transfer  $S_\theta$  and viscous dissipation  $S_\psi$  for  $n = 0.6, 1.0,$  and  $1.4$  in the concentric cylindrical annulus under non-uniform sinusoidal inner-wall heating ( $\theta = 0.5(1 + \sin \varphi)$ ). For  $n = 0.6$ ,  $S_\theta$  is highly localized in the upper annular region where the imposed temperature gradient is maximum, consistent with the asymmetric isotherm clustering observed in Fig. 16, while  $S_\psi$  remains the dominant irreversibility source; however, both its peak magnitude and spatial extent are considerably reduced compared to the uniform heating case (Fig. 19), reflecting the confinement of vigorous convective motion to localized angular regions under the sinusoidal thermal forcing. At  $n = 1.0$ , both  $S_\theta$  and  $S_\psi$  decrease noticeably, with entropy contours concentrated near the heated inner wall, consistent with the weakened circulation ( $|\psi|_{\max} = 9.64$ ) in Fig. 16; the reduction in  $S_\psi$  is more pronounced than that in  $S_\theta$  relative to Fig. 19, highlighting the stronger suppression of large-scale convective motion under non-uniform heating. For  $n = 1.4$ , both entropy components are significantly diminished, with  $S_\theta$  confined to a thin layer adjacent to the inner wall and  $S_\psi$  appearing only in small isolated zones,

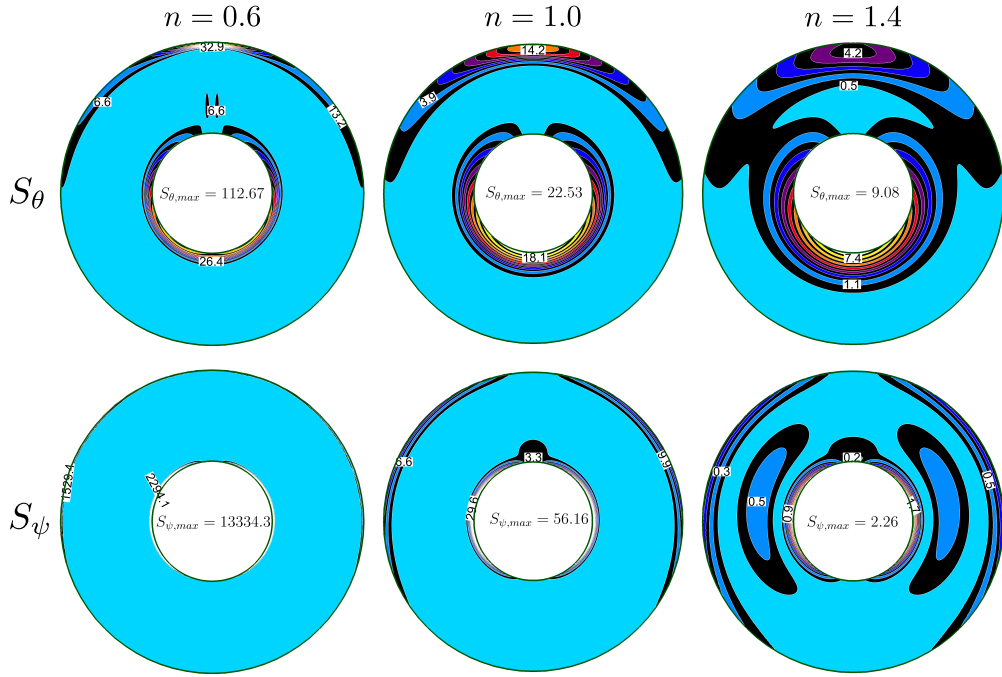


**Figure 19:** Contours of local entropy generation due to heat transfer  $S_\theta$  (top) and fluid friction  $S_\psi$  (bottom) for power-law indices  $n = 0.6, 1.0,$  and  $1.4$  in the concentric cylindrical annulus with uniform bottom-wall heating ( $\theta = 1$ ).

**Table 4**

Total entropy generation due to heat transfer ( $S_{\theta,\text{total}}$ ), fluid friction ( $S_{\psi,\text{total}}$ ), combined total entropy generation ( $S_{\text{total}}$ ), and average Bejan number ( $\text{Be}_{\text{av}}$ ) for power-law indices  $n = 0.6, 1.0,$  and  $1.6$  in the concentric cylinder annulus under uniform and non-uniform inner-wall heating.

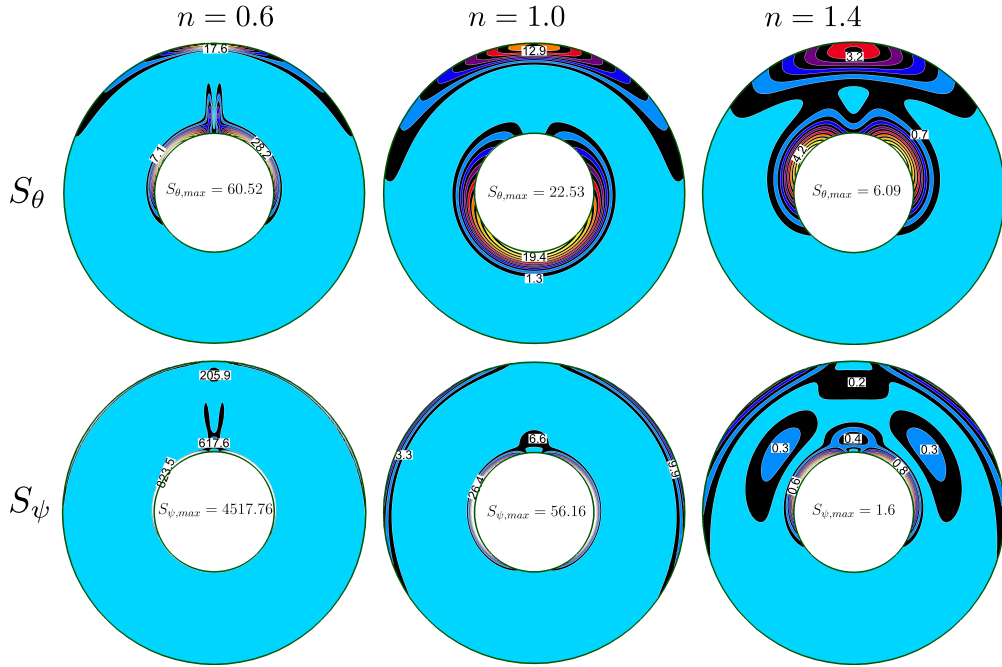
Uniform heating inner wall				
$n$	$S_{\theta,\text{total}}$	$S_{\psi,\text{total}}$	$S_{\text{total}}$	$\text{Be}_{\text{av}}$
0.6	29.11686473	820.908914	850.025787	0.0342540961241055
1.0	13.89810836	15.43842255	29.33653091	0.473747506
1.6	8.514377316	1.452288412	9.966665728	0.85428543

Non-uniform heating inner wall				
$n$	$S_{\theta,\text{total}}$	$S_{\psi,\text{total}}$	$S_{\text{total}}$	$\text{Be}_{\text{av}}$
0.6	12.31946233	280.5788535	292.8983158	0.042060543
1.0	6.093160385	6.603836072	12.69699646	0.479889902
1.6	3.711581468	0.683463739	4.395045207	0.844492216

consistent with the weak velocity gradients and near-conduction regime evident in Fig. 16; the dominance of  $S_\theta$  over  $S_\psi$  at this  $n$ -value confirms a complete transition to heat-transfer-dominated irreversibility.

Table 4 quantifies  $S_{\theta,\text{total}}$ ,  $S_{\psi,\text{total}}$ ,  $S_{\text{total}}$ , and  $\text{Be}_{\text{av}}$  for the concentric cylindrical annulus under both heating configurations. Under uniform heating, the shear-thinning fluid ( $n = 0.6$ ) yields the highest  $S_{\text{total}} = 850.03$ , overwhelmingly dominated by viscous dissipation ( $S_{\psi,\text{total}} = 820.91$ ,  $\text{Be}_{\text{av}} = 0.034$ ), consistent with the extremely large and spatially widespread  $S_\psi$  contours observed in Fig. 19, where intense circulation and strong velocity gradients drive irreversibility throughout the annular domain. As  $n$  increases to 1.0,  $S_{\text{total}}$  drops sharply to 29.34 with a more balanced contribution between  $S_{\theta,\text{total}} = 13.90$  and  $S_{\psi,\text{total}} = 15.44$  ( $\text{Be}_{\text{av}} = 0.474$ ), reflecting the moderate and localized entropy contours in Fig. 19. For  $n = 1.6$ ,  $S_{\psi,\text{total}}$  reduces drastically to 1.45, driving  $\text{Be}_{\text{av}}$  to 0.854 and confirming a near-complete transition to heat-transfer-dominated irreversibility, corroborated by the weak and confined



**Figure 20:** Contours of local entropy generation due to heat transfer  $S_\theta$  (top) and fluid friction  $S_\psi$  (bottom) for power-law indices  $n = 0.6, 1.0,$  and  $1.4$  in the concentric cylindrical annulus with non-uniform sinusoidal heating ( $\theta = 0.5(1 + \sin \varphi)$ ).

$S_\psi$  contours in Fig. 19. Under non-uniform heating, the same rheological trend persists but with substantially reduced absolute values across all  $n$ ; notably, for  $n = 0.6$ ,  $S_{\text{total}}$  decreases from 850.03 to 292.90 and  $\text{Be}_{\text{av}}$  remains low (0.042), confirming that viscous dissipation continues to dominate but is spatially confined to localized angular regions, as evidenced by the reduced  $S_\psi$  contour extent in Fig. 20. The near-identical  $\text{Be}_{\text{av}}$  values across both heating cases for  $n = 1.0$  and  $n = 1.6$  confirm that the power-law index, rather than the thermal boundary condition, governs the transition from viscous- to heat-transfer-dominated irreversibility in the annular configuration.

This trend is further quantified in Fig. 21, where the total entropy generation  $S_{\text{total}}$  decreases sharply with increasing power-law index  $n$  for both heating conditions, with consistently lower values observed under non-uniform heating due to spatial localization of thermal forcing. Conversely, the average Bejan number  $\text{Be}_{\text{av}}$  increases monotonically with  $n$ , indicating a progressive shift from viscous-dominated irreversibility to heat-transfer-dominated behavior. Notably, the close agreement between uniform and non-uniform heating curves for  $\text{Be}_{\text{av}}$  suggests that the rheological effects dominate the irreversibility mechanism, while thermal boundary conditions primarily influence its magnitude rather than its nature.

## 7. Concluding remarks and outlook

This study examined the role of thermal boundary conditions on natural convection and entropy generation in non-Newtonian power-law fluids confined within a square cavity and a concentric cylindrical annulus. A `Gridap.jl` finite element framework was developed for the steady two-dimensional governing equations under the Boussinesq approximation and validated against established benchmark solutions for both Newtonian and non-Newtonian cases. The good agreement obtained for isotherm fields, streamlines, local Nusselt number distributions, and entropy generation contours confirms the accuracy and robustness of the present numerical methodology.

The results demonstrate that thermal boundary conditions strongly influence the structure and intensity of buoyancy-driven transport, while their interaction with fluid rheology governs the resulting thermodynamic irreversibility. Uniform heating promotes stronger and more spatially distributed circulation, yielding higher heat transfer rates and larger total entropy generation. In contrast, non-uniform sinusoidal heating localizes the thermal forcing, confines plume development to restricted regions, and consistently reduces the total entropy generation in both geometries. At the same time, the power-law index remains a key controlling parameter: shear-thinning fluids enhance

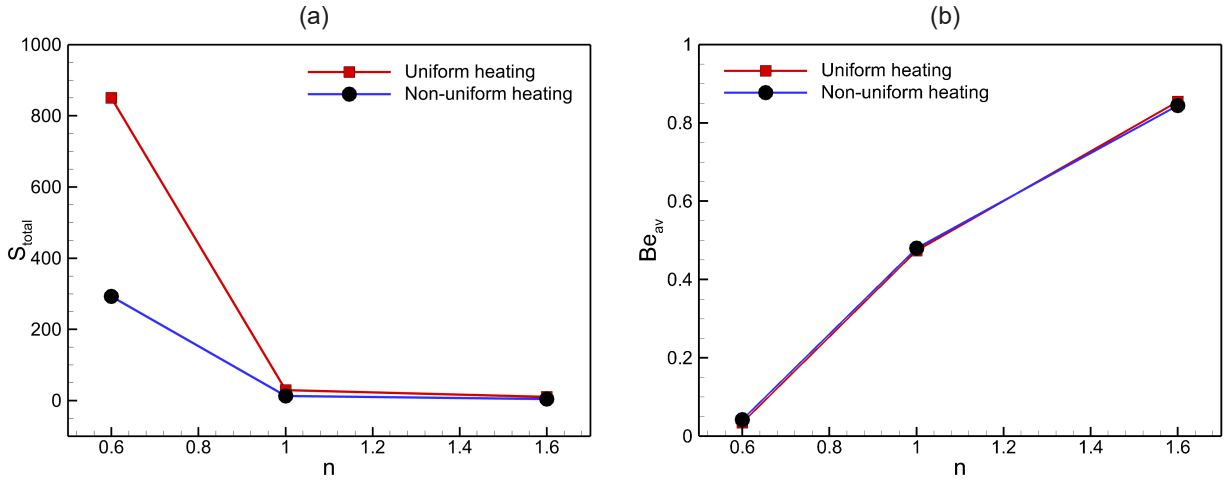


**Figure 21:** Variation of (a) total entropy generation  $S_{\text{total}}$  and (b) average Bejan number  $Be_{\text{av}}$  with power-law index  $n$  in the concentric cylindrical annulus under uniform ( $\theta = 1$ ) and non-uniform ( $\theta = 0.5(1 + \sin \varphi)$ ) inner wall heating.

convection and intensify thermal and velocity gradients, whereas shear-thickening fluids suppress circulation and shift the system toward conduction-dominated behavior.

Entropy generation analysis further shows that the dominant source of irreversibility depends primarily on the rheological nature of the fluid, whereas the imposed thermal boundary condition determines its magnitude and spatial distribution. In shear-thinning fluids, viscous dissipation contributes significantly to the total irreversibility, particularly in the annular geometry where circulation is strongest. As the power-law index increases, the contribution of fluid-friction irreversibility decreases rapidly, and the Bejan number rises, indicating a transition toward heat-transfer-dominated entropy generation. The findings highlight that thermal boundary design offers an effective means of controlling heat transfer performance and thermodynamic losses in systems involving power-law fluids. Future work may extend the present framework to three-dimensional flows, higher Rayleigh number regimes, and more complex constitutive models, as well as to optimization strategies for thermally efficient systems with non-Newtonian working fluids.

## Acknowledgments

L.T. acknowledges the support by the German Research Foundation (DFG), project B04 (504291427) within the SFB 1481 (442047500). S.S. acknowledge the support by the German Research Foundation (DFG), within the Research Unit FOR5409 under project number 463312734.

## Data availability & reproducibility

We provide the source code, scripts, and data to reproduce the simulations results on GitHub (<https://github.com/lamB000/GeMotion.jl>) and Zenodo [57].

## A. Appendix: Nomenclature

$u, v$	Velocity components in $x$ and $y$ directions (m/s)
$U, V$	Dimensionless velocity components
$x, y$	Cartesian coordinates (m)
$X, Y$	Dimensionless coordinates
$r, \varphi$	Cylindrical radial and angular coordinates (m, rad)
$p$	Pressure (Pa)
$P$	Dimensionless pressure
$T$	Temperature (K)
$\theta$	Dimensionless temperature
$T_h$	Hot wall temperature (K)
$T_c$	Cold wall temperature (K)
$\psi$	Stream function
$\Pi$	Heat function
$\Phi_i$	Basis function in finite element formulation
$\tau_{ij}$	Shear stress tensor components (Pa)
$\mu_a$	Apparent viscosity (Pa·s)
$\alpha$	Thermal diffusivity (m <sup>2</sup> /s)
$\nu$	Kinematic viscosity (m <sup>2</sup> /s)
$K$	Consistency index in power-law fluid (Pa·s <sup><math>n</math></sup> )
$n$	Power-law index
$\rho$	Fluid density (kg/m <sup>3</sup> )
$\beta$	Thermal expansion coefficient (1/K)
$g$	Gravitational acceleration (m/s <sup>2</sup> )
$\hat{g}$	Dimensionless buoyancy direction vector
$L$	Characteristic length (m)
$R_i$	Inner cylinder radius (m)
$R_o$	Outer cylinder radius (m)
Ra	Rayleigh number
Pr	Prandtl number
Nu	Nusselt number
$Nu_b, Nu_s$	Local Nusselt number at bottom and side walls
$Nu_{avg}$	Average Nusselt number
$S_\theta$	Local entropy generation due to heat transfer
$S_\psi$	Local entropy generation due to fluid friction
$S_{\theta, total}$	Total entropy generation from heat transfer
$S_{\psi, total}$	Total entropy generation from fluid friction
$S_{total}$	Total entropy generation
$Be_{av}$	Average Bejan number
$\phi$	Irreversibility distribution parameter

## B. Appendix: Variational formulation and finite element discretization

The variational formulation is derived in a general form so that it can be applied to the square cavity, the annular domain, and more general two-dimensional geometries  $\Omega \subset \mathbb{R}^2$ . The boundary  $\Gamma = \partial\Omega$  is decomposed as  $\Gamma = \Gamma_D \cup \Gamma_N$ , with  $\Gamma_D \cap \Gamma_N = \emptyset$ , in order to accommodate Dirichlet and Neumann boundary conditions in a unified manner. For the derivation, a vector notation is adopted by introducing  $\mathbf{U} := (\mathbf{U}, P, \theta) := ((U, V), P, \theta)$  as the vector of unknown fields. Furthermore, the gradient operator is denoted by  $\nabla := (\partial_X, \partial_Y)^\top$ , and the divergence of the velocity field is written as  $\nabla \cdot \mathbf{U} = \partial_X U + \partial_Y V$ . The outward unit normal vector on the boundary is denoted by  $\mathbf{n}$ .

The steady, dimensionless governing equations for incompressible natural convection of a power-law fluid from (10)–(13) can then be written as

$$\left\{ \begin{array}{l} \nabla \cdot \mathbf{U} = 0 \text{ in } \Omega, \\ (\mathbf{U} \cdot \nabla)\mathbf{U} + \nabla P - 2 \text{Pr} \nabla \cdot (\bar{\mu}_s(\nabla\mathbf{U})D(\nabla\mathbf{U})) - \text{Ra Pr} \theta \hat{\mathbf{g}} = \mathbf{0} \text{ in } \Omega, \\ \mathbf{U} \cdot \nabla\theta - \nabla \cdot (\nabla\theta) = 0 \text{ in } \Omega, \\ \mathbf{U} = \mathbf{0} \text{ on } \Gamma, \nabla\theta \cdot \mathbf{n} = 0 \text{ on } \Gamma_N, \theta = \theta_D \text{ on } \Gamma_D. \end{array} \right. \quad (48)$$

In Eq. (48),  $\mathbf{U} = (U, V)$ ,  $P$ , and  $\theta$  denote the dimensionless velocity, pressure, and temperature fields, respectively. No-slip and impermeability conditions are imposed on the entire boundary  $\Gamma$ , whereas the thermal boundary conditions are prescribed through a mixed Dirichlet–Neumann description:  $\theta = \theta_D$  on  $\Gamma_D$  and  $\nabla\theta \cdot \mathbf{n} = 0$  on the adiabatic part  $\Gamma_N$ . The vector  $\hat{\mathbf{g}}$  denotes the dimensionless buoyancy direction defined in Sec. 2.4. To avoid singularities when  $|\nabla\mathbf{U}| \rightarrow 0$ , we stabilize the dimensionless apparent viscosity by introducing a small regularization parameter  $c_{\text{stab}} > 0$  and use

$$\bar{\mu}_s(\nabla\mathbf{U}) = (c_{\text{stab}} + 2D(\nabla\mathbf{U}) : D(\nabla\mathbf{U}))^{\frac{n-1}{2}}, \quad c_{\text{stab}} = 10^{-3}. \quad (49)$$

The trial space is denoted by  $\mathbb{U}$  and includes the prescribed velocity and temperature Dirichlet data. The corresponding test space is denoted by  $\mathbb{V}$ , with homogeneous conditions on the Dirichlet boundaries; the pressure component is constrained to have zero mean. For each  $\mathbf{U} \in \mathbb{U}$ , we introduce a test function  $\mathcal{V} = (\mathbf{v}, q, \zeta) \in \mathbb{V}$ . We then multiply (48) by their respective test functions and integrate over  $\Omega$ . Integration by parts and summing all equations leads to the following nonlinear variational problem: Find  $\mathbf{U} = (\mathbf{U}, P, \theta) \in \mathbb{U}$ , such that for all  $\mathcal{V} = (\mathbf{v}, q, \zeta) \in \mathbb{V}$ :

$$R((\mathbf{U}, P, \theta), (\mathbf{v}, q, \zeta)) = a((\mathbf{U}, P, \theta), (\mathbf{v}, q, \zeta)) + b_U(\mathbf{v}) + c_U(\mathbf{v}) + d_{U,\theta}(\zeta) = 0, \quad (50)$$

with the bilinear form

$$a((\mathbf{U}, P, \theta), (\mathbf{v}, q, \zeta)) = - \int_{\Omega} (\nabla \cdot \mathbf{v})P \, d\Omega + \int_{\Omega} (\nabla \cdot \mathbf{U})q \, d\Omega + \int_{\Omega} \nabla\theta \cdot \nabla\zeta \, d\Omega - \text{Ra Pr} \int_{\Omega} \theta \hat{\mathbf{g}} \cdot \mathbf{v} \, d\Omega, \quad (51)$$

and the  $\mathbf{U}$ -dependent semilinear forms for viscous diffusion, convective momentum transport, and energy transport,

$$b_U(\mathbf{v}) = 2 \text{Pr} \int_{\Omega} \bar{\mu}_s(\nabla\mathbf{U}) (D(\nabla\mathbf{v}) : D(\nabla\mathbf{U})) \, d\Omega, \quad c_U(\mathbf{v}) = \int_{\Omega} ((\mathbf{U} \cdot \nabla)\mathbf{U}) \cdot \mathbf{v} \, d\Omega, \quad d_{U,\theta}(\zeta) = \int_{\Omega} (\mathbf{U} \cdot \nabla\theta)\zeta \, d\Omega. \quad (52)$$

We note here, that for the Newtonian case, i.e.,  $n = 1$ , the form  $b(\mathbf{U}, \mathbf{v}) := b_U(\mathbf{v})$  is bilinear and resembles the classical viscous term in the Navier–Stokes equations since the apparent viscosity is constant.

For the nonlinear residual  $R(\mathbf{U}, \mathcal{V})$  from the weak form (50), given a starting point  $\mathbf{U}_0$ , we write  $\mathbf{U}_{k+1} = \mathbf{U}_k + \delta\mathbf{U}_k$  [56, p324ff]. The linearization of  $R$  yields the Jacobian

$$R'_{\mathbf{U}_k}(\delta\mathbf{U}_k, \mathcal{V}) = a(\delta\mathbf{U}_k, \mathcal{V}) + db(\mathbf{U}_k, \delta\mathbf{U}_k, \mathbf{v}) + dc(\mathbf{U}_k, \delta\mathbf{U}_k, \mathbf{v}) + dd(\mathbf{U}_k, \delta\mathbf{U}_k, \theta_k, \delta\theta_k, \zeta). \quad (53)$$

The viscous contribution to the Jacobian involves the derivative of the power-law viscosity:

$$db(\mathbf{U}_k, \delta\mathbf{U}_k, \mathbf{v}) = \int_{\Omega} 2 \text{Pr} [d\bar{\mu}_s(\nabla\mathbf{U}_k; \nabla\delta\mathbf{U}_k)D(\nabla\mathbf{U}_k) + \bar{\mu}_s(\nabla\mathbf{U}_k)D(\nabla\delta\mathbf{U}_k)] : D(\nabla\mathbf{v}) \, d\Omega. \quad (54)$$

To derive the explicit expression for  $d\bar{\mu}_s$ , we apply the chain rule to the stabilized apparent viscosity definition. Let  $\gamma(\nabla\mathbf{U}) = c_{\text{stab}} + 2[D(\nabla\mathbf{U}) : D(\nabla\mathbf{U})]$  be the regularized shear-rate magnitude. Then, in the direction  $\nabla\delta\mathbf{U}$ , we have

$$d\bar{\mu}_s(\nabla\mathbf{U}; \nabla\delta\mathbf{U}) = \frac{n-1}{2} \gamma(\nabla\mathbf{U})^{\frac{n-3}{2}} 4 (D(\nabla\mathbf{U}) : D(\nabla\delta\mathbf{U})). \quad (55)$$

This derivative accounts for the nonlinear dependence of the apparent viscosity on the velocity gradient, which is essential for the Newton–Raphson convergence. For  $n < 1$ , the negative exponent in the regularized shear-rate invariant

makes the viscosity derivative especially sensitive in low-shear regions. For  $n = 1$ , the derivative vanishes and the Newtonian case reduces to a constant-viscosity contribution.

The convective terms contribute with

$$dc(\mathbf{U}_k, \delta\mathbf{U}_k, \mathbf{v}) = \int_{\Omega} ((\mathbf{U}_k \cdot \nabla) \delta\mathbf{U}_k) \cdot \mathbf{v} \, d\Omega + \int_{\Omega} ((\delta\mathbf{U}_k \cdot \nabla) \mathbf{U}_k) \cdot \mathbf{v} \, d\Omega, \quad (56)$$

while the thermal advection contribution is

$$dd(\mathbf{U}_k, \delta\mathbf{U}_k, \theta_k, \delta\theta_k, \zeta) = \int_{\Omega} (\delta\mathbf{U}_k \cdot \nabla \theta_k) \zeta \, d\Omega + \int_{\Omega} (\mathbf{U}_k \cdot \nabla \delta\theta_k) \zeta \, d\Omega. \quad (57)$$

The resulting Newton update rule per iteration is given by the solution to the following linear system: Find  $\delta\mathbf{U}_k$ , such that

$$\mathbf{R}'_{\mathcal{U}_k}(\delta\mathcal{U}_k, \mathcal{V}) = -\mathbf{R}(\mathcal{U}_k, \mathcal{V}) \quad \forall \mathcal{V} \in \mathbb{V} \quad (58)$$

In the discrete setting, this translates to solving the linear system  $\mathbf{J}^{(k)} \delta\mathbf{U}_h^{(k)} = -\mathbf{R}^{(k)}$ , where  $\mathbf{J}^{(k)}$  is the assembled Jacobian matrix,  $\delta\mathbf{U}_h^{(k)}$  is the vector of degrees of freedom for the Newton update, and  $\mathbf{R}^{(k)}$  is the residual vector. After solving for  $\delta\mathbf{U}_h^{(k)}$ , the new iterate is computed as  $\mathbf{U}_h^{(k+1)} = \mathbf{U}_h^{(k)} + \delta\mathbf{U}_h^{(k)}$ .

## References

- [1] F. P. Incropera, Convection heat transfer in electronic equipment cooling, *J. Heat Transfer* 110 (1988) 1097–1111. doi:10.1115/1.3250613.
- [2] M.M. Al-Hazmy, Analysis of coupled natural convection–conduction effects on the heat transport through hollow building blocks, *Energy Build.* 38 (5) (2006) 515–521. doi:10.1016/j.enbuild.2005.08.010.
- [3] S. Ali, A.M. Sadoun, A. Fathy, A.W. Abdallah, Numerical modeling of magnetohydrodynamic buoyancy-driven convection for enhanced energy applications, *Case Stud. Therm. Eng.* 52 (2023) 103823. doi:10.1016/j.csite.2023.103823.
- [4] M.F. Pakdaman, A. Lashkari, H. Basirat Tabrizi, R. Hosseini, Performance evaluation of a natural-convection solar air-heater with a rectangular-finned absorber plate, *Energy Convers. Manage.* 52 (2) (2011) 1215–1225. doi:10.1016/j.enconman.2010.09.017.
- [5] J.K. Novev, R.G. Compton, Natural convection effects in electrochemical systems, *Curr. Opin. Electrochem.* 7 (2018) 118–129. doi:10.1016/j.coelec.2017.09.010.
- [6] A. Bejan, *Convection Heat Transfer*, 4th ed., Wiley, New York, 2013. doi:10.1002/9781118671627.
- [7] V.V. Calmidi, R.L. Mahajan, Forced convection in high porosity metal foams, *J. Heat Transfer* 122 (3) (2000) 557–565. doi:10.1115/1.1287793.
- [8] H. Buchberg, I. Catton, D.K. Edwards, Natural convection in enclosed spaces – a review of application to solar energy collection, *J. Heat Transfer* 98 (2) (1976) 182–188. doi:10.1115/1.3450516.
- [9] L. Theisen, Automated boundary layer mesh generation for simulation of convective cooling, B.Sc. Thesis, RWTH Aachen University, 2018. doi:10.18154/RWTH-2023-12261.
- [10] A. Guha, K. Pradhan, Natural convection of non-Newtonian power-law fluids on a horizontal plate, *Int. J. Heat Mass Transf.* 70 (2014) 930–938. doi:10.1016/j.ijheatmasstransfer.2013.11.001.
- [11] L. Yang, K. Du, A comprehensive review on the natural, forced, and mixed convection of non-Newtonian fluids (nanofluids) inside different cavities, *J. Therm. Anal. Calorim.* 140 (5) (2020) 2033–2054. doi:10.1007/s10973-019-08987-y.
- [12] A.V. Shenoy, R.A. Mashelkar, Thermal convection in non-Newtonian fluids, *Adv. Heat Transfer* 15 (1982) 143–225. doi:10.1016/S0065-2717(08)70174-6.
- [13] K. Khanafer, K. Vafai, M. Lightstone, Buoyancy-driven heat transfer enhancement in a two-dimensional enclosure utilizing nanofluids, *Int. J. Heat Mass Transf.* 46 (19) (2003) 3639–3653. doi:10.1016/S0017-9310(03)00156-X.
- [14] R.B. Bird, R.C. Armstrong, O. Hassager, *Dynamics of Polymeric Liquids, Vol. 1: Fluid Mechanics*, Wiley, New York, 1987.
- [15] R.P. Chhabra, J.F. Richardson, *Non-Newtonian Flow and Applied Rheology: Engineering Applications*, Butterworth-Heinemann, Oxford, 2010. doi:10.1016/B978-0-7506-8532-0.X0001-7.
- [16] R.I. Tanner, *Engineering Rheology*, 2nd ed., Oxford University Press, Oxford, 2000. doi:10.1093/oso/9780198564737.001.0001.
- [17] A.B. Metzner, J.C. Reed, Flow of non-Newtonian fluids – correlation of the laminar, transition, and turbulent-flow regions, *AIChE J.* 1 (4) (1955) 434–440. doi:10.1002/aic.690010409.
- [18] M. Hatami, D.D. Ganji, Natural convection of sodium alginate (SA) non-Newtonian nanofluid flow between two vertical flat plates by analytical and numerical methods, *Case Stud. Therm. Eng.* 2 (2014) 14–22. doi:10.1016/j.csite.2013.11.001.
- [19] L. Khezdar, D. Siginer, I. Vinogradov, Natural convection of power law fluids in inclined cavities, *Int. J. Therm. Sci.* 53 (2012) 8–17. doi:10.1016/j.ijthermalsci.2011.10.020.
- [20] M.R. Safaei, B. Rahmadian, M. Goodarzi, Numerical study of laminar mixed convection heat transfer of power-law non-Newtonian fluids in square enclosures by finite volume method, *Int. J. Phys. Sci.* 6 (33) (2011) 7456–7470. doi:10.5897/ijps11.1092.
- [21] A.B. Metzner, Heat transfer in non-Newtonian fluids, *Adv. Heat Transfer* 2 (1965) 357–397. doi:10.1016/S0065-2717(08)70264-8.

- [22] T. Basak, S. Roy, A.R. Balakrishnan, Effects of thermal boundary conditions on natural convection flows within a square cavity, *Int. J. Heat Mass Transf.* 49 (23–24) (2006) 4525–4535. doi:10.1016/j.ijheatmasstransfer.2006.05.015.
- [23] T. Basak, S. Roy, T. Paul, I. Pop, Natural convection in a square cavity filled with a porous medium: effects of various thermal boundary conditions, *Int. J. Heat Mass Transf.* 49 (7–8) (2006) 1430–1441. doi:10.1016/j.ijheatmasstransfer.2005.09.018.
- [24] S. Roy, T. Basak, Finite element analysis of natural convection in a square cavity with non-uniformly heated wall(s), *Int. J. Eng. Sci.* 43 (8–9) (2005) 668–680. doi:10.1016/j.ijengsci.2005.01.002.
- [25] M. Sathiyamoorthy, T. Basak, S. Roy, I. Pop, Steady natural convection flows in a square cavity with linearly heated side wall(s), *Int. J. Heat Mass Transf.* 50 (3–4) (2007) 766–775. doi:10.1016/j.ijheatmasstransfer.2006.06.019.
- [26] R. Nouri, et al., Non-Newtonian natural-convection in a square box submitted to horizontal heat flux and magnetic field, *Therm. Sci.* 28 (4A) (2024) 3049–3061. doi:10.2298/TSCI231030079N.
- [27] X. Pan, P. Wang, Y. Zhang, J. Song, B. Yang, Thermal convection characteristics of different thermal boundary condition defining methods in an aircraft cabin, *Appl. Therm. Eng.* 266 (2025) 125646. doi:10.1016/j.applthermaleng.2025.125646.
- [28] T. Basak, S. Roy, C. Thirumalesha, Finite element analysis of natural convection in a triangular enclosure: effects of various thermal boundary conditions, *Chem. Eng. Sci.* 62 (9) (2007) 2623–2640. doi:10.1016/j.ces.2007.01.053.
- [29] A. M’hadbi, M. El Ganaoui, H.B. Hamed, A. Guizani, K. Chtaibi, Natural convection of a power-law nanofluid in a square cavity with a vertical fin, *Fluid Dyn. Mater. Process.* 20 (9) (2024) 2091–2108. doi:10.32604/fdmp.2024.050763.
- [30] T. Basak, S. Roy, Role of ‘Bejan’s heatlines’ in heat flow visualization and optimal thermal mixing for differentially heated square enclosures, *Int. J. Heat Mass Transf.* 51 (13–14) (2008) 3486–3503. doi:10.1016/j.ijheatmasstransfer.2007.10.033.
- [31] N. Rehman, R. Mahmood, A.H. Majeed, I. Khan, A. Mohamed, Multigrid simulations of non-Newtonian fluid flow and heat transfer in a ventilated square cavity with mixed convection and baffles, *Sci. Rep.* 14 (1) (2024) 6694. doi:10.1038/s41598-024-57322-5.
- [32] T. Basak, S. Roy, S.K. Singh, I. Pop, Effects of thermal boundary conditions on entropy generation during natural convection, *Numer. Heat Transf. A* 59 (5) (2011) 372–402. doi:10.1080/10407782.2011.549075.
- [33] F.T. Mahmood, A. Das, T.S. Chowdhury, M.N. Hasan, Thermo-hydraulic perspectives of non-Newtonian channel flow with active flow modulation: A CFD study, *J. Non-Newtonian Fluid Mech.* 339–340 (2025) 105416. doi:10.1016/j.jnnfm.2025.105416.
- [34] A. Bejan, Entropy generation minimization: the method of thermodynamic optimization of finite-size systems and finite-time processes, CRC Press, 1995. doi:10.1201/9781482239171.
- [35] A. Bejan, A study of entropy generation in fundamental convective heat transfer, *J. Heat Transf.* 101 (4) (1979) 718–725. doi:10.1115/1.3451063.
- [36] H.F. Oztop, K. Al-Salem, A review on entropy generation in natural and mixed convection heat transfer for energy systems, *Renew. Sustain. Energy Rev.* 16 (1) (2012) 911–920. doi:10.1016/j.rser.2011.09.012.
- [37] M.H. Matin, I. Pop, S. Khanchezar, Natural convection of power-law fluid between two-square eccentric duct annuli, *J. Non-Newtonian Fluid Mech.* 197 (2013) 11–23. doi:10.1016/j.jnnfm.2013.02.002.
- [38] S. Saouli, S. Aiboud-Saouli, Second law analysis of laminar falling liquid film along an inclined heated plate, *Int. Commun. Heat Mass Transf.* 31 (6) (2004) 879–886. doi:10.1016/S0735-1933(04)00074-0.
- [39] S. Mahmud, R.A. Fraser, Second law analysis of heat transfer and fluid flow inside a cylindrical annular space, *Exergy Int. J.* 2 (4) (2002) 322–329. doi:10.1016/S1164-0235(02)00078-X.
- [40] A. Acrivos, M.J. Shah, E.E. Petersen, Momentum and heat transfer in laminar boundary-layer flows of non-Newtonian fluids past external surfaces, *AIChE J.* 6 (2) (1960) 312–317. doi:10.1002/aic.690060227.
- [41] H. Ozoe, S.W. Churchill, Hydrodynamic stability and natural convection in Ostwald–de Waele and Ellis fluids: the development of a numerical solution, *AIChE J.* 18 (6) (1972) 1196–1207. doi:10.1002/aic.690180617.
- [42] O. Turan, A. Sachdeva, N. Chakraborty, R.J. Poole, Laminar natural convection of power-law fluids in a square enclosure with differentially heated sidewalls subjected to constant temperatures, *J. Non-Newton. Fluid Mech.* 166 (17–18) (2011) 1049–1063. doi:10.1016/j.jnnfm.2011.06.003.
- [43] O. Turan, A. Sachdeva, R.J. Poole, N. Chakraborty, Laminar natural convection of power-law fluids in a square enclosure with differentially heated sidewalls subjected to constant wall heat flux, *J. Heat Transf.* 134 (12) (2012) 122504. doi:10.1115/1.4007123.
- [44] G.B. Kim, J.M. Hyun, H.S. Kwak, Transient buoyant convection of a power-law non-Newtonian fluid in an enclosure, *Int. J. Heat Mass Transf.* 46 (19) (2003) 3605–3617. doi:10.1016/S0017-9310(03)00149-2.
- [45] M. Lamsaadi, M. Naimi, M. Hasnaoui, Natural convection of non-Newtonian power law fluids in a shallow horizontal rectangular cavity uniformly heated from below, *Heat Mass Transf.* 41 (3) (2005) 239–249. doi:10.1007/s00231-004-0530-8.
- [46] S. Badia, F. Verdugo, Gridap: An extensible finite element toolbox in Julia, *J. Open Source Softw.* 5 (52) (2020) 2520. doi:10.21105/joss.02520.
- [47] F. Verdugo, S. Badia, The software design of Gridap: A finite element package based on the Julia JIT compiler, *Comput. Phys. Commun.* 276 (2022) 108341. doi:10.1016/j.cpc.2022.108341.
- [48] J. Bezanson, A. Edelman, S. Karpinski, V.B. Shah, Julia: A fresh approach to numerical computing, *SIAM Rev.* 59 (1) (2017) 65–98. doi:10.1137/141000671.
- [49] P.K. Mogensén, K. Carlsson, S. Villemot, S. Lyon, M. Gomez, C. Rackauckas, T. Holy, D. Widmann, T. Kelman, D. Karrasch, A. Levitt, A.N. Riseth, C. Lucibello, C. Kwon, D. Barton, Julia TagBot, M. Baran, M. Lubin, S. Choudhury, S. Byrne, S. Christ, T. Arakaki, T.A. Bojesen, benneti, M.R. Guzmán Macedo, JuliaNLSolvers/NLsolve.jl: V4.5.1, Zenodo (2020). doi:10.5281/zenodo.4404703.
- [50] T. Basak, S. Roy, Role of Bejan’s heatlines in heat flow visualization and optimal thermal mixing for differentially heated square enclosures, *Int. J. Heat Mass Transf.* 51 (13–14) (2008) 3486–3503. doi:10.1016/j.ijheatmasstransfer.2007.10.033.
- [51] T. Basak, S. Roy, I. Pop, Heat flow analysis for natural convection within trapezoidal enclosures based on heatline concept, *Int. J. Heat Mass Transf.* 52 (11–12) (2009) 2471–2483. doi:10.1016/j.ijheatmasstransfer.2009.01.020.

- [52] V.A.F. Costa, Bejan's heatlines and masslines for convection visualization and analysis, *Appl. Mech. Rev.* 59 (3) (2006) 126–145. doi:10.1115/1.2177684.
- [53] R.S. Kaluri, T. Basak, Entropy generation minimization versus thermal mixing due to natural convection in differentially and discretely heated square cavities, *Numer. Heat Transf. A: Appl.* 58 (6) (2010) 475–504. doi:10.1080/10407782.2010.511982.
- [54] O. Turan, A. Sachdeva, N. Chakraborty, R.J. Poole, Laminar natural convection of power-law fluids in a square enclosure with differentially heated side walls subjected to constant temperatures, *J. Non-Newton. Fluid Mech.* 166 (17–18) (2011) 1049–1063. doi:10.1016/j.jnnfm.2011.06.003.
- [55] M.H. Matin, W.A. Khan, Laminar natural convection of non-Newtonian power-law fluids between concentric circular cylinders, *Int. Commun. Heat Mass Transf.* 43 (2013) 112–121. doi:10.1016/j.icheatmasstransfer.2013.02.006.
- [56] H. C. Elman, D. J. Silvester, A. J. Wathen, *Finite Elements and Fast Iterative Solvers: With Applications in Incompressible Fluid Dynamics, Numerical Mathematics and Scientific Computation*, Oxford University Press, Oxford; New York, 2005. doi:10.1093/oso/9780198528678.001.0001.
- [57] L. Theisen, S. Singh, Gemotion.jl: A Julia finite-element solver for steady two-dimensional Navier–Stokes–Fourier natural-convection problems with generalized material laws, *Zenodo*, v0.1.2 (2026). doi:10.5281/zenodo.20128652.